NUMERICAL INVESTIGATION OF THE DYNAMICS LEADING TO TORNADOGENESIS IN A SUPERCELL ENVIRONMENT

By

SCOTT T. TREVORROW

A Thesis submitted in partial fulfillment of

the requirements for the degree of

Master of Science

(Atmospheric and Oceanic Sciences)

at the

UNIVERSITY OF WISCONSIN-MADISON

2014

ABSTRACT

This thesis investigates the dynamical processes leading to tornadogenesis in a supercell thunderstorm through numerical simulation of a full-physics idealized supercell, and supporting simulations of a downdraft plume, independent of the full supercell environment. Numerical simulations and observations of pre-tornadogenesis environments have shown vortex features arching over and forming a couplet of vorticity that straddles the rear flanking cold pool of supercell storms. Present-day paradigms that explain this kinematic field fail to explain the recognized importance of certain diagnostic tornadogenesis parameters, namely 0-1 km Storm Relative Helicity. The results of experiments performed in this thesis reveal the role that a barotropic vortex sheet roll-up process has in forming vortices that can become the core of a developing tornado vortex. The observed kinematic environment during this process resembles that of current vortex line arching paradigms since developing vortices along the Rear Flanking Gust Front are vertically erect and arch in a similar manner. It is therefore proposed that an alternative conceptual model for explaining the existence of arched vortex lines may include the elementary arguments of non-supercell tornadogenesis and vertical wind shear tilting by the storm's Rear Flanking Downdraft. A discussion and graphical illustration of this conceptual model is provided in the conclusion.

ACKNOWLEDGEMENTS

I must first thank the numerous mentors and peers in the University of Wisconsin – Madison's Atmospheric and Oceanic Sciences department that have advised me throughout my academic tenure at the UW. Without their persistent guidance and fellowship, I am confident that my efforts related to this degree and its associated research would have not reached the conclusion they have.

Chief of these is my advisor, Professor Greg Tripoli. I feel incredibly fortunate to have been able to perform research under Greg's mentorship. Since first meeting him, he has found a way to push me to work harder, think deeper, and see farther than the current state of my understanding. It is without question that, if I am fortunate enough to achieve success as an atmospheric scientist in the future, it is a consequence of the time I have spent working with Greg as a graduate student. I cannot express my gratitude enough for the patience he has shown me as I work through the growing pains of becoming an effective communicator, his willingness to sacrifice his valuable time to teach me concepts I am ignorant of, and for investing his resources in order to support my advancement as a scientist. Thank you.

I thank Professor Jon Martin and Professor Matt Hitchman, who dedicated their time and effort to read this thesis in its final stages of completion. I hold their perspectives in the highest regard and I am honored that they would consider it worth their time to read through and comment on the many pages of this text.

In addition, I feel the need to address a few other individuals, specifically. Richard

Hildner's guidance in the beginning stages of my Master's degree program set my research goals and focus in the direction they are today. I thank him for his patience and his coaching. Marcus Büker has not only been a valued advisor, but a generous supporter. He, in essence, took my under his wing as I gave my first live oral presentation at the 26th Severe Local Storms Conference in Nashville, Tennessee during my first semester as a graduate student. I am confident that the magnitude of composure I possessed while presenting was entirely a function of his willingness to personally introduce me to the conference environment and I thank him immensely for that. Recently, my office-mate and fellow research partner Luke Odell has been subject to numerous requests to read and edit versions of the journal paper I am writing in association with the work presented in this thesis. He is always willing to give great advice and have conversations with me that have the potential to last for hours. I thank him for his patience as well as his insightful commentary. Finally, I owe a huge debt to Croix Christensen who, throughout the thesis writing process, has been an enormous help by being willing to answer formatting questions and by offering his formatted thesis as a skeleton for my own. Without his help, I simply would not have been able to complete this thesis by its due date.

It would be an injustice to not acknowledge the aid of Pete Prokrandt. From setting up the NMS on NCAR's supercomputers, to answering numerous Vis5D questions and helping set up this thesis' defense presentation, Pete has been an integral part of this thesis' conclusion. I know I am forgetting many other instances where his help was essential in maintaining the progress of this research, and in doing so I fear that I am not giving him the full recognition he deserves. However, with all sincerity, I am incredibly thankful for

all Pete has done and I thank him in advance for his future assistance.

I must also thank my family for their guidance and encouragement, not only as a graduate student, but also throughout my entire life. They have tried to instill in me the character traits of perseverance, hard work, respect, responsibility and humility. As I grow older and more mature in the field of atmospheric science, it becomes increasingly obvious that these character traits define those of an effective scientist and leader. While I often struggle, I continue to strive for excellence in these areas. Not only because of my career pursuit in atmospheric science, but because I am constantly reminded of the importance of such qualities in a husband, a father, and a member of society. I thank them for continuing to hold me accountable to such a standard.

Finally, and most importantly, I must thank my wife, Brianne. There is no unit of measurement that can accurately gauge the debt I owe her for her unfailing love, unwavering support, and selfless sacrifice throughout this entire process. She is, and always will be, my life's inspiration.

The National Science Foundation (NSF) financially sponsored this research through the Grant, AGS-1137137.

TABLE OF CONTENTS

LIST OF FIGURES

A three-dimensional isosurface of total vorticity magnitude equal to .05 s^{-1} colored the same as Figure 1b viewed from the South. The white oval is used to draw attention to the partially rolled-up, arched vortex tube it encircles while the vertical scale bar gives perspective of the height of the arched tube, roughly 1.5 km. (b) Same as (a) with the total vorticity isosurface removed. The orange, near-surface streamlines provide a visualization of the horizontal shear instability along the RFGF roughly 100 m from the ground. (c) A top-down view of the RFGF and the associated 100 m AGL vertical vorticity field colored as in Figure 3.1b. The white circle encompasses the same arched tube in (a) and (b). Black lines indicate contours of zero vertical vorticity. (d) A time series of vertical vorticity along the magenta line indicated in (c) between points A and B from 3000-3300 s into the NMS-Id simulation. The center of the tube in (c) is the center of the instability in (d).

Figure 3.3: Vertical cross section through the instability along the RFGF at the same simulation time as Figure 2. The cross section shows a quantity calculated as $w \cdot \left(\partial v/\partial x - \partial u/\partial y\right)$, which is the vertical stretching of surface-based, vertically oriented vorticity since vertical motion is zero at the surface. (a) Looking down at the surface-level equivalent potential temperature colored as in Figure 3.1a, the magenta line shows the orientation of the cross section. (b) The vertical stretching quantity cross section as viewed from the South. Magenta contours show lines of constant vertical stretching quantity at .5 m s^{-2} intervals to manifest an area of maximum stretching through the instability. The core of this quantity's maximum shown in (b) is > 3.0 m s^{-2} and its height is roughly 1.5 km.

Figure 3.4: An oblique view from the North of the arched vortex tube while being stretched vertically as a result of the arched vortex tube's interaction with the supercell's updraft 3400 s after model initiation. To cleanly view the vortex tube as it was stretched vertically, rendered total vorticity isosurfaces west of the vortex tube were clipped out of the image. The dotted line in the center of the image shows from what point the image was clipped. The horizontal cross section is the same as in Figure 3.1 and the three-dimensional isosurface is the same as in Figure 3.2a. The white arrow is used to indicate the region of stretching by the updraft. Measured vertical vorticity values at the core of the funnel were .24 s^{-1}.

Figure 3.5: An oblique view from the South of a mature vortex funnel 4200 s into the NMS-Id simulation. The horizontal cross section is as Figure 3.1 and the three-dimensional isosurface shows a three-dimensional vorticity magnitude equal to 2.5 s^{-1}, colored as in Figure 3.1b. Core vertical vorticity inside the vortex was found to be approximately .6 s^{-1}.

Figure 4.1: A graphical illustration of the anticipated relationship between vertically-oriented vorticity observed along the leading edge of an outflow boundary and vertical wind shear. In both illustrations, an idealized environment characterized by south-southeasterly low-level winds (brown arrow) and westerly mid-level winds is assumed. The westerly mid-level winds are brought to the surface by means of the RFD establishing the outflow boundary of interest. In addition, the outflow's momentum is illustrated using

blue vectors (whose magnitudes can be determined via the provided scale at the top-left corner of each image). Vectors colored in red illustrate southerly gust-front-relative environmental winds. The gray area in each image indicates the RFGF transition zone between the westerly momentum of the cold outflow and the south-southeasterly momentum of the low-level environment. In each of the following cases, the change in wind shear is assumed to be a result of increasing the mid-level winds and not the low-level environmental wind, which remains fixed. (a) In the case of a low-level wind shear layer characterized by a *straight-line hodograph*, convergence along the RFGF is enhanced as the cold outflow intercepts strong south-southeasterly low-level flow. Horizontal shear along the density current interface manifests itself as a sheet of positive, cyclonic vorticity and the transition zone's width is minimized due to enhanced convergence. Strong, but small and numerous vortex features develop within the transition zone in this environment. (b) In the case of a low-level wind shear layer characterized by a *clockwise-curved hodograph*, the outflow intercepts the same low-level environment but with relatively weaker convergence. Even though horizontal shear across the density current interface still manifests itself as a sheet of cyclonic vertical vorticity, the width of the transition zone is larger because of the weaker convergence. With the added support of storm-relative helicitiy, a few relatively large vortex features develop within the transition zone in this environment. If downdraft-induced wind shear and helicity tilting is responsible for the low-level kinematic features in the NMS-Id simulation, this relationship should be obvious in the idealized downdraft experiments.

Figure 4.2: Hodographs for each of the horizontally homogeneous vertical wind shear profiles used in the idealized downdraft simulations. (a) A completely static initialization. (b) A linear, unidirectional sheared vertical wind profile where westerly momentum increases from 0–1 km in the domain. The symbol "G" indicates the motion of the model grid. (c) An idealized, directionally sheared vertical wind profile where relatively weak southerly flow increases in magnitude and veers with increasing height to a southwesterly orientation at mid-levels (above 1 km). The symbol "G" is the same as in (b).

Figure 4.3: Three-dimensional isosurfaces of -0.1 K potential temperature in the (a) NS-E, (b) US-E and (c) DS-E simulations at times 9 min (*top row*), 15 min (*second row*), 23 min (*third row*) and 27 min (*bottom row*) from model initiation as viewed from the South. In all of the images, surface potential temperature is plotted as a colored horizontal cross section whose temperature scale can be seen at the bottom of each column of images. Black boxes with an area of roughly 1 km^2 are plotted against the surface potential temperature horizontal cross section to provide a sense of spatial scale.

Figure 4.4: Three-dimensional isosurfaces of .04 s^{-1} total vorticity magnitude in the (a) NS-B, (b) US-B and (c) DS-B simulations at times 9 min (*top row*), 15 min (*second row*), 23 min (*third row*) and 27 min (*bottom row*) from model initiation as viewed from the South. These isosurfaces are colored as in Figure 3.1b. In all of the images, surface potential temperature is plotted as a colored horizontal cross section whose temperature scale can be seen at the bottom of each column of images. Black boxes with an area of

roughly 1 km^2 are plotted against the surface potential temperature horizontal cross section to provide a sense of spatial scale.

Figure 4.5: Same as Figure 4.4 except the three-dimensional isosurface value of total vorticity has been increased to .02 s^{-1} and the simulated domain is viewed from a Notheastern vantage point. Also observe the change in simulation time for each image in (a) and (b).

Figure 4.6: A top view of the (a) US-E and (b) DS-E simulated domains 13 min (*top row*) and 19 min (*bottom row*) after model initiation. The background in each image is colored by surface potential temperature and the foreground color in each image corresponds to near-surface (less than 300 m AGL) vertical vorticity values of $> 0.1\ s^{-1}$ (red) and vertical vorticity values $< -0.1\ s^{-1}$ (blue). The "C" and "A" labels in each image stand for "cyclonic" and "anticyclonic", respectively.

Figure 4.7: A comparison between the predicted and final results of the idealized downdraft simulations. (*Top Row*) The predicted results as they were presented in Figure 4.1. (*Bottom Row*) The downdraft experiment results after 23 min of simulation time as they were presented in Figure 4.5. (*Left Column*) Environments with a unidirectionally sheared, or straight-line hodograph, low-level wind profile. (*Right Column*) Environments with a directionally sheared, or clockwise-curved hodograph, low-level wind profile.

Figure 4.8: A comparison between the vertical stretching of vortex sheet roll-ups in the the NMS-Id simulation and the DS-E idealized downdraft simulation. (*Left Column*) The NMS-Id results are presented as they were in Figure 3.3. (*Right Column*) The DS-E idealized downdraft results as they were presented in Figure 4.6 with a vertical cross section (magenta line) of the same stretching quantity shown in Figure 3.3. Note the vertical height of the roll up in the DS-E simulation is half that of the roll-up in the NMS-Id simulation.

Figure 5.1: Same as in Figure 4.4, but for each of the experiments performed using the bubble perturbation with the three different 0-1 km vertical wind shear profiles in Figure 4.2. (a) No wind shear. (b) Straight-line hodograph. (c) Clockwise-curved hodograph. The symbol "d" in (c) is used to show the depth of the vortex sheet which is approximately 250 m. Notice these figures appear much more clean than in Figure 4.3, owing to the fact that cold air is not consistently being generated aloft in this sensitivity experiment.

Figure 5.2: Same as in Figure 5.1 but using the disk cooling function thermal perturbation. The symbol "d" in (c) is used to show the depth of the outflow boundary vortex sheet, which is approximately 500 m. This is roughly equivalent to that of the DS-E simulation (Fig. 4.4c) and twice that of the DS-B simulation (Fig. 5.1c).

Figure 5.3: (a) Hodograph representing the vertical wind shear layer prescribed for the sensitivity experiment where the depth of the shear layer is increased from 1 km to 2 km.

(b) Hodograph from the original DS-E simulation using a 0-1 km wind shear layer. The green fill shows the 0-1 km Storm Relative Helicity (SRH) characteristic of this wind shear layer. (c) Same hodograph as in (a) with its 0-1 km SRH shown in green fill. Notice the shape and orientation of the hodograph remains unchanged between (b) and (c) and it is only the depth of the layer that is modified. This effectively decreases the 0-1 km SRH in the deep shear layer case (compare (b) to (c)).

Figure 5.4: (a) DS-E simulation results showing (*top-row*) the thermal perturbation evolution after 23 min and 27 min of simulation time, and (*bottom row*) the vorticity evolution displayed as in Figure 5.2 after 23 min and 27 min of simulation time. (b) Same as (a), but for the simulation using a deeper shear layer (Fig. 5.3a). Notice there appears to be more vertically oriented vorticity situated along the eastward edge of the outflow boundary in (a) as opposed to (b).

Figure 5.5: (a) Northeastern view of the DS-E simulation's vorticity evolution, as shown in Figure 4.5, 23 min and 27 min into the simulation. (b) Same as (a) but for the simulation using a deeper wind shear layer (Fig. 5.3a). Notice the vorticity distribution along the northeastern edge of the outflow boundary in (b) after 27 min of simulation time appears quite similar to the US-E simulation in Figure 4.5a.

Figure 5.6: (a) DS-E simulation results as shown in Figure 5.4a. (b) DS-E simulation results displayed as in (a) after 23 min and 27 min of simulation time when a surface friction parameterization defined by Louis (1979) was turned on. The symbols "d_0" in (a) and "d_1" in (b) are used to show the depth of their corresponding vortex sheets. After investigating these values it was found that, d_0 was roughly 500 m and d_1 was roughly 250m.

Figure 6.1: Vertical cross sections illustrating the RFGF vortex sheet's genesis where the thick magenta line indicates a single environmental vortex line of the ambient wind shear's vortex sheet. Viewing perspective is from the South. Vectors tails and heads indicate wind velocity into and out of the page, respectively. The small box in the bottom right-hand corner of the figure is a *top-down* view showing the orientation of the cross sections (magenta line) relative to a rear flanking cold pool in (c). In a storm-relative environment of a traditional right-moving supercell, as a Rear Flanking Downdraft (RFD) subsides into the environment below the supercell thunderstorm upstream (to the west) of the mesocyclone (a) it brings mid-level momentum to the surface (b) where, along the outflow boundary, the ambient vertical wind shear is focused as an arched vortex sheet with positive vertical vorticity along the gust front (c). The vertical orientation and arching of the sheet is a consequence of the density current leading head's circulation.

Figure 6.2: (a) see Figure 1.1a. (b) See Figure 1.1b. (c) A conceptual model built to represent the pre-tornadogenesis dynamics discussed in this text using vortex lines. As a downdraft subsides into a storm-relative environment characterized by positive low-level SRH, wind shear and helicity tilting by the downdraft yields a vertically erect vortex sheet

along the outflow's gust front that arches back over the cold pool. As the vortex sheet rolls-up, support from the low-level SRH helps intensify resulting vortex tubes that are situated beneath the mesocyclone aloft. This acts to aggregate surrounding low-level vertical vorticity at the same time that the vortex arches become more vertically erect, due to vertical stretching. The consequent distribution of low-level vorticity is then a couplet of cyclonic and anticylonic vorticity that straddles the surface cold pool and is associated with vertically arching vortex lines.

Chapter 1 – Introduction

Tornadoes are violent and potentially catastrophic meteorological phenomena that predominantly affect the United States, but have been recorded on almost every continent (Fujita 1973). From their place in early Native American culture as *horse spirits* (Marchand 1993) to the silver screen in modern American popular culture, tornadoes and their parent supercell storms have become integrated into the fabric of the societies routinely exposed to them. However, despite cultural recognition of these severe weather events over the centuries, it has only been since the 1950s that significant progress has been made in understanding their dynamics and forecasting their genesis.

a. A Brief, Pre-1950 History of Tornadogenesis Research and Forecasting

The first recorded attempts at understanding tornado initiation in order to produce tornado forecasts (or "*predictions*" as they were called) were in 1884 by an officer in the Army Signal Corps with a passion for tornadoes named John Park Finley (Finley 1884; Schaefer 1986). Without any real means of observation other than recruited spotters scattered across the United States, he forecasted favorable and unfavorable tornado potentials for the eastern half of the country using pattern recognition on large-scale weather maps (Finley 1888; Galway 1985). While his method of verification was a pioneering effort, his research and work was eventually terminated after losing support from his superiors (Galway 1985). Very little tornado research was performed in the United States from then and on into the mid-20th century (Doswell 2007). Out of the 131 papers presented at national meetings from officials of the civilian-run Weather Bureau in

1898, 1901 and 1904, none were related to tornadoes (Bradford 1999). However, as the nation grew, a growing anxiety toward their devastating effects followed.

Without real-time observations, or a general understanding of tornadic storms, the word "tornado" was banned from public forecast discussions prior to 1950 by the Signal Corps and the Weather Bureau in an effort to prevent public panic (Doswell et al. 1993). However, motivated by the military's entry into World War II, meteorological research of severe weather began to accelerate given the threat that severe weather posed to military installations and munitions plants (Corfidi 1999). It was at this time that research into the development and evolution of thunderstorms via the "Thunderstorm Project" (Byers and Braham 1949) was underway. This Congressionally mandated, multi-agency field campaign ultimately paved the way for severe storms research by emphasizing the practicality and importance of field observations in understanding deep convection. It was also at this time that two Air Force officers, Ernest Fawbush and Robert Miller stationed at Tinker Air Force Base in Oklahoma, accomplished what would become known as the first operational tornado forecast. Although Fawbush and Miller integrated current theory into their analysis, their methodology remained relatively unchanged from Finley's nearly 60 years earlier. Using large-scale pattern recognition, they were able to accurately predict the occurrence of a tornado in the Tinker Air Force Base area on 25 March 1948, just 5 days after the same region suffered $10 milllion in damage from a previous tornado event (Grice et al. 1999; Miller and Crisp 1999).

b. Early Supercell and Tornadogenesis Theory

The success of Fawbush and Miller, in tandem with better observations owing to new radar technology, had a tangible influence on the Weather Bureau who lifted the ban on the word "tornado" in their public weather forecasts in 1952 (Dowell et al. 1993). This effectively opened the door for future systematic research into the evolution of tornadic storms. In 1953, the first radar observations of tornadic storms showed the existence of hook echoes in association with an observed surface tornado vortex (Bluestein 2010). At the same time, groundbreaking still and motion picture filming of tornadogenesis events by Theodore Fujita captured characteristics of the tornado environment never before seen in the field of meteorology (Doswell 2007). Fujita was therefore forced to invent new terminology to represent his observations and he consequently developed a new conceptual model for tornadic storms that would later become recognized as the *supercell* (Fujita 1960). It is hard to overstate Fujita's contribution to tornado research even at such an early stage of the science's evolution. In addition to his revolutionary tornado classification scheme using damage as a proxy for wind speed, some of the original terminology from his supercell model, mainly "*wall*" and "*tail*" cloud, are still used with relatively little controversy today (Doswell 2007).

In the late 1950s, perhaps in response to Fujita's work, there was a particular focus on the evolution of the tornado's parent, supercell storm. Chester and Harriet Newton were the first to suggest the potential relationship between vertical wind shear and deep, isolated convective updraft propagation (Newton and Newton 1959) after similar work showed the relationship between upper level winds and the movement of large rainstorms (Newton and Katz 1958). Their argument, in support of a pre-existing knowledge of

similar dynamics in long-lived, large-scale convective systems (Desai and Mal 1938; Humphreys 1940; Newton 1950) was that low-level outflow at the base of isolated deep convection could initiate convection favorably along its leading (storm-relative downshear) boundary. This concept was carried with Neil Ward in 1961 when, in participation with the National Severe Storms Project (NSSP), made the first scientific tornado chase (Bluestein 2010). Based on his visual observations, he postulated that the cold outflow of the tornado's parent storm played a role in the tornado's genesis (Ward 1961). While there was no theoretical explanation as to why the low-level outflow was important to tornadogenesis, it nonetheless indicated that there was an ordered sequence of events leading up to tornadogenesis initiation (Browning and Donaldson 1963).

c. Foundational Tornadogenesis Paradigms

With the aid of Doppler radar, the NEXRAD array, more powerful numerical models and more scientifically-based storm chasing, the 1970s and 1980s were somewhat of a revolutionary time period for tornado research (Doswell 2007). The integrated use of these tools provided enhanced observational data, which helped reveal the complex dynamics of tornadogenesis and pre-tornadogenesis environments. Resulting paradigms developed in this time frame would become the foundation for future tornadogenesis research and understanding.

Throughout the 1970s, analysis of proximity sounding data highlighted a relationship between wind shear and the severity of ensuing weather, especially tornado-producing storms (e.g. Barnes 1970; Maddox 1976; Darkow and McCann 1977). Maddox (1976) went further to mention the noticeable relationship between the storm-relative

winds of a right-moving supercell and tornadogenesis; a relationship also manifested in new Doppler imagery of tornadic storms (e.g. Ray et al. 1975; Ray 1976). Numerical studies around this time (e.g. Lin and Chang 1977; Wilhelmson and Klemp 1978) verified the relationship between environmental wind shear and right-moving supercell storms that were responsible for the storm-relative winds predominantly associated with tornadic environments. Then, drawing on this work and other studies throughout the decade, Lemon and Doswell (1979) produced the first three-dimensional conceptual model of the tornadic supercell that is still widely used today to illustrate the storm's structure and explain its low-level environment.

The 1970s also brought about advancements in the understanding of tornadogenesis in non-supercell environments. Perhaps the most foundational study at the time was by Maxworthy (1973) who discussed the role of ambient vertical wind shear tilting by a boundary layer thermal in forming dust-devil-like atmospheric vortices. Using field observations and laboratory studies he concluded that, once initiated, a dust devil could prolong its lifecycle by moving right of the mean wind. He argued that such a motion enhanced the *Storm Relative Helicity (SRH)* defined as,

$$SRH = \int \left(\vec{V}_h - \vec{C} \right) \cdot \nabla \times \vec{V}_h \, dz \,, \tag{1}$$

where $\vec{V}_h$ is horizontal wind, $\vec{C}$ is storm/cloud motion relative to the ground and z is height above the ground. In this way, a dynamical connection between tornadoes in non-supercell and supercell environments was revealed.

Meanwhile, laboratory vortex chamber experiments (see Ward 1972) of non-supercellular atmospheric vortices showed a relationship between vortex structure and an empirically derived ratio between the vortex's tangential velocity (v_0) and mean vertical velocity ($\overline{w}$) defined as,

$$S \equiv \frac{v_0}{\overline{w}} \tag{2}$$

(Davies-Jones 1973; Rotunno 1977; Rotunno 1978; Church et al. 1979; Rotunno 1982; Gall 1983). This parameter, called the *swirl ratio*, experimentally demonstrated the importance of helicity for maintaining vortex strength and longevity. Church et al. (1979) and those investigating swirl ratio in laboratory experiments submitted that swirl ratio was not a governing characteristic of the flow, but it still provided a useful diagnostic for a vortex's structure. It continues to be used as such today (Lewellen and Lewellen 2007), although with some appreciable resistance from the academic community who argue that its dependence on Reynolds number (Stokes 1851; Reynolds 1883) and its diagnostic nature make it a less-than-ideal parameter in atmospheric vortex analyses (e.g. Nolan 2006).

In the 1980s, more research related to non-supercell tornadogenesis revealed that shear-lines on the edge of thunderstorm outflows rolled-up to form centers of high vorticity (e.g. Bluestein 1980; Bluestein 1985). This was consistent with field campaigns in south Florida a decade earlier that showed a similar process along the convergence zone of sea breezes resulting in the formation of waterspouts and relatively weak tornadoes (Golden 1971; Golden 1974). It also supported the work of Barcilon and Drazin (1972) who argued

that the development of dust devils and similar atmospheric vortices could be explained by invoking the fluid dynamics of *vortex sheets*. These thin, free shear layer surfaces mark the transition between two fluid streams and often become established along convergence zones where the tangential flow across the zone boundary is discontinuous (Krasny 1988). This makes them inviscidly unstable to perturbations of any wavelength (Batchelor 1967, Wu et al. 2006). Barotropic, Kelvin-Helmholtz-type instabilities along the sheet can then grow at the expense of the background kinetic energy, if its growth tendency overcomes any viscous damping, and effectively roll the sheet up into a focused center of vorticity via a *vortex sheet roll-up process* (Drazin and Howard 1966). To date, this process continues to be the seminal theoretical paradigm for non-supercell tornadogenesis after being verified in numerous studies of weak tornadic vortices over the following decades (Wakimoto and Wilson 1989; Lee and Wilhelmson 1997a,b; Marquis et al. 2007).

With the exception of a few relatively recent studies (Bluestein et al. 2003; Noda and Niino 2005; Noda and Niino 2010; Lee et al. 2012) the vortex sheet roll-up process was not used to explain tornadogenesis in a supercell environment. Therefore, in the 1980s the problem remained that for tornadogenesis to occur, vertical vorticity must somehow be introduced at the surface where it was initially absent. With this in mind, two predominant theories emerged.

The first was actually proposed at the end of the 1970s and eventually became known as the "*dynamic pipe effect*" (DPE) theory (Leslie and Smith 1978). Put briefly, DPE theory suggested that, for a mesocyclone in cyclostrophic balance, the vertical pressure gradient force at its base would draw air vertically upward through its core. In

this event, DPE theory asserted that a responding circulation at the mesocyclone's base must arise in order to maintain cyclostrophic balance. This would effectively lower the vorticity of the mesocyclone toward the ground and, along with it, the vertical pressure gradient force at its base. Downward propagation via this process would continue until the mesocyclone makes contact with the surface, at which point the vertical pressure gradient force could no longer draw air through the center of the vortex from below. While DPE theory did provide a testable hypothesis for how vertical vorticity could be introduced at the surface, Doppler studies of tornadogenesis both supported and opposed this theory depending on the specific tornadogenesis event (e.g. Trapp and Davies-Jones 1997). Furthermore, very recent literature suggests that DPE may be a misrepresentation of the true tornadogenesis dynamics at work (French et al. 2013).

The second proposed theory that explained the introduction of surface vorticity in order to achieve tornadogenesis was actually more an affirmation of the previous works of Newton and Newton (1959) and Ward (1961). Davies-Jones (1982a,b) suggested that, in the absence of appreciable surface vertical vorticity, a downdraft was needed for tornadogenesis. With the help of numerical simulations (e.g. Klemp and Rotunno 1983), research continued to support the idea that a downdraft was likely an important component for tornadogenesis in a supercell environment. However, at the time, there was no principal explanation as to why.

d. Current Tornadogenesis Theory

While it has been recognized that pre-tornadogenesis environments lacking low-level (less than 1 km) rotation need a downdraft to instigate tornadogenesis since the

1980s, the process, or interaction of processes, by which a downdraft triggers tornadogenesis is still not entirely understood (Davies-Jones et al. 2001; Markowski and Richardson 2009). Based on the foundational work of Klemp and Rotunno (1983), initial theories at the turn of the century have suggested that, in environments characterized by vertical wind shear, ambient horizontal vorticity can be tilted vertically downward by means of a downdraft (Davies-Jones and Brooks 1993; Walko 1993; Davies-Jones et al. 2001). This is analogous to mesocyclone formation (see Davies-Jones 1984; Rotunno and Klemp 1985) and introduces near-surface vertically oriented vorticity where it was initially absent (Fig. 1.1a).

However, ambient horizontally oriented vorticity is not the only source of vorticity in this environment. Because of a downdraft's thermodynamic nature, *solenoidally* (or *baroclinically*) generated vorticity is also present. Via the solenoidal term in the vorticity tendency equation, assuming a circular shaped downdraft domain, this vorticity manifests itself as a horizontally oriented ring vortex around the downdraft's periphery. This is an additional source of vorticity that can be locally tilted and subsequently stretched by an updraft when either a downdraft subsides along the updraft boundary (Fig. 1.1b) or an emanating vortex ring associated with the storm's surface propagating outflow is caught in the storm's low-level inflow (Klemp and Rotunno 1983; see Fig. 1.1c). These processes ultimately lead to the introduction of vertically-oriented vorticity in the form of a couplet of cyclonic and anticyclonic vorticity near the surface (Straka et al. 2007 (S07)). S07 discussed the likely prominence of these processes due to the large body of dual-Doppler observations showing low-level, counter-rotating vortices that straddle the cold outflow of

supercell thunderstorms (e.g. Brandes 1984; Bluestein et al. 1996; Wakimoto et al. 1998; Wakimoto and Cai 2000; Bluestein and Gaddy 2001).

Further investigation of low-level vorticity introduction processes via a supercell's Rear Flanking Downdraft (RFD) in simulated and observed pre-tornadogenesis environments have led to the use of vortex lines as a diagnostic tool (e.g. S07; M08; Markowski et al. 2012a, 2012b). The benefit of using vortex lines in a qualitative, diagnostic analysis is that they behave as material surfaces in a barotropic and inviscid fluid (Wu et al. 2006). Therefore, observing the evolution of their orientation while calculating the tendency of vorticity along them is an informative way of studying the dynamics of tornadogenesis and pre-tornadogenesis environments.

Analyses of vortex lines associated with the supercell's RFD in observational and numerical studies of tornadogenesis have shown a consistent trend in their orientation. That is, vortex lines appear to originate near the Rear Flanking Gust Front (RFGF) with positive vertical vorticity and arch over the cold pool associated with the RFD (e.g. M08; see Fig. 1.2). This is in contrast to what is expected if ambient, horizontal vortex lines suspended above the surface are depressed downward by the RFD. Therefore, M08 proposes that the arched vortex lines are an indication that solenoidally, or baroclinically, generated vorticity on the periphery of the storm's outflow is the primary source of low-level rotation leading to tornadogenesis.

Of the only two hypotheses presented by S07 that produce the observed pre-tornadogenesis kinematic environment and include a downdraft's baroclinic vorticity, recent literature has proven that only one is physically possible. Tilting of the storm's

surface propagating outflow by its low-level inflow (Fig. 1.1c) *cannot* effectively produce low-level couplets of vorticity. Due to a build up of higher pressure along the downshear, low-level environment side of the cold outflow boundary, air is forced vertically upward in advance of the outflow boundary. Consequently, this inhibits upward vertical tilting of the outflow's horizontally oriented vorticity that is situated behind/upshear-of the outflow boundary (Markowski and Davies-Jones 2013). Therefore, the only remaining paradigm that explains the importance of a downdraft in instigating tornadogenesis, the observed arched vortex lines, and the couplets of vorticity, is that which invokes a baroclinic *updraft-downdraft interaction.* Specifically, tilting of baroclinically generated vorticity in the RFD via the mesocyclone's main updraft and the region downstream of the main RFD's subsidence core is theorized to generate the low-level couplet of cyclonic and anticyclonic vertically oriented vorticity noted by S07. Associated vortex line arches are then situated suitably for further stretching and intensification by the storm's updraft. This paradigm, referred to as *vortex line arching* theory, is widely accepted in current literature as the process by which vortex lines become arched and vorticity couplets are produced.

Considering this theory for a moment, it is reasonable to therefore deduce that the RFD's baroclinicity magnitude is proportional to the magnitude of low-level rotation observed and ultimately the probability of tornadogenesis occurring. However, despite the RFD's role in low-level vorticity introduction, growing evidence suggests that strong cold pools and strong negative buoyancy near the surface are unfavorable for tornadogenesis (Markowski et al. 2002; Shabbott and Markowski 2006; Grzych et al. 2007; Marquis et al. 2012). M08 suggests that the baroclinicity of the RFD must therefore be a "goldilocks"

type of problem where some is necessary, but too much implies a rapidly propagating gust front that can inhibit vorticity stretching and result in a low-level environment resembling a Fujita microburst model (Fujita 1985, Proctor 1988).

Furthermore, vortex line arching theory does not explicitly explain why low-level environments characterized by strong, positive, low-level Storm Relative Helicity (SRH; see Eq. 1.1) are favorable for tornadogenesis (Markowski et al. 2003). The RFD's baroclinically generated vorticity is tilted vertically upward by the updraft aloft and not at the ground, such that low-level flow into the base of the mesocyclone does not explicitly penetrate the RFD's baroclinically generated vorticity. Thus, tilting of the RFD's vorticity does not explicitly benefit from the low-level SRH. This realization fosters a motivation to find an alternative explanation for the kinematic field observed prior to tornadogenesis that justifies the importance of favorable, pre-tornadogenesis environmental characteristics, namely 0-1 km SRH.

e. Thesis

Using vortex-line arching theory, current literature suggests that the tilting and stretching of a downdraft's baroclinically generated vorticity via an *updraft-downdraft interaction* is the most likely source of low-level, vertically-oriented vorticity prior to tornadogenesis (M08, Markowski et al. 2012a). However, using vortex lines as a diagnostic tool for this analysis may overlook existing vortex-on-vortex interactions since, via Helmholt'z theorem, they fail to represent material surfaces in the presence of baroclinic vorticity production. Focusing primarily on an updraft-downdraft interaction may also obscure key insights regarding the downdraft's role in tornadogenesis by

overlooking the physical, kinematic interactions that exist between the downdraft's baroclinically generated vorticity and the low-level ambient vertical wind shear. It may then prove fruitful to study the low-level vorticity evolution resulting from a downdraft's subsidence within an ambient, vertical wind shear alongside an updraft's interaction with the downdraft's baroclinic vorticity. Such a process may prove to benefit from the SRH characteristic of the environment as well. *Therefore, it is the hypothesis of this thesis that ambient horizontal vorticity tilting by the RFD is an important dynamical process leading to tornadogenesis in a supercell storm.*

This thesis is organized such that, in Chapter 2, the general methodology of this study is discussed starting with a description of the numerical model employed. Chapter 3 discusses the results of an idealized tornado producing supercell simulation that yielded the pre-tornadogenesis dynamics from which this thesis is motivated. Chapter 4 is dedicated to the design and results of simple toy model simulations that expose the role of downdraft-induced wind shear tilting in the pre-tornadogenesis dynamics of the idealized tornado supercell simulation. Chapter 5 is dedicated to the setup and results of sensitivity experiments performed against the toy model results featured in Chapter 4. Finally, in Chapter 6, a concluding discussion is given that synthesizes this thesis' findings and discusses their relevance with respect to the current state of the science. A graphical illustration of this study's proposed pre-tornadogenesis dynamics in the idealized tornado supercell simulation is also given as a new conceptual model for tornadogenesis in a supercell environment.

Chapter 1 Figures

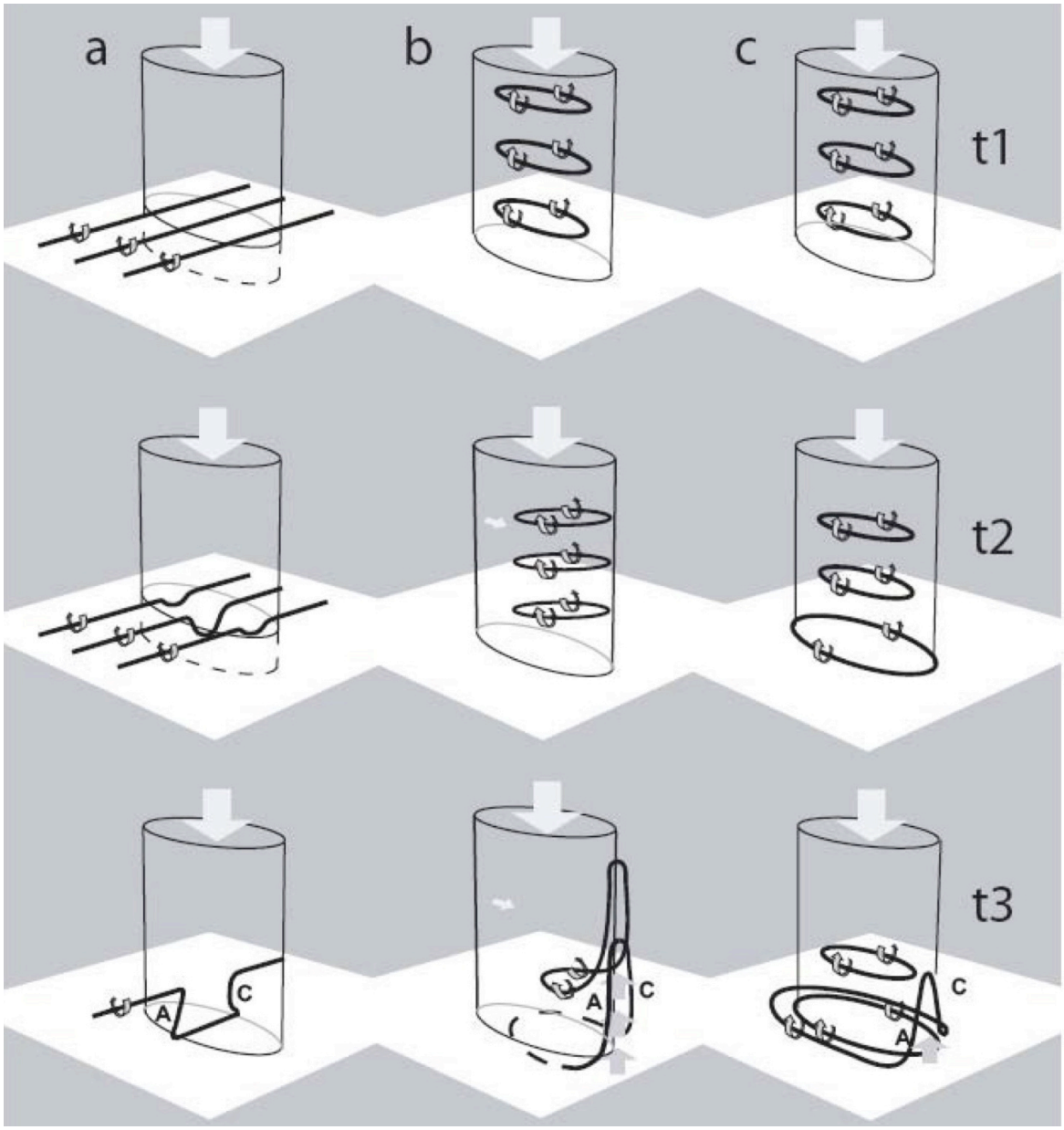

Figure 1.1: Conceptual models of the dynamics resulting in near-surface vorticity couplets that straddle the rear flanking surface cold pool of supercell thunderstorms as illustrated by Straka et al. (2007). Solid black lines in each image are vortex lines with orientations given by the arrows curling around each vortex line. (a) Downdraft tilting of environmental vertical wind shear (Walko 1993). (b) The *updraft-downdraft interaction* process showing local tilting and stretching of a downdraft's baroclinically produced vorticity by an updraft aloft (Markowski et al. 2008). (c) Localized tilting of the surface-propagating outflow's horizontal vorticity by the low-level inflow (Klemp and Rotunno 1983).

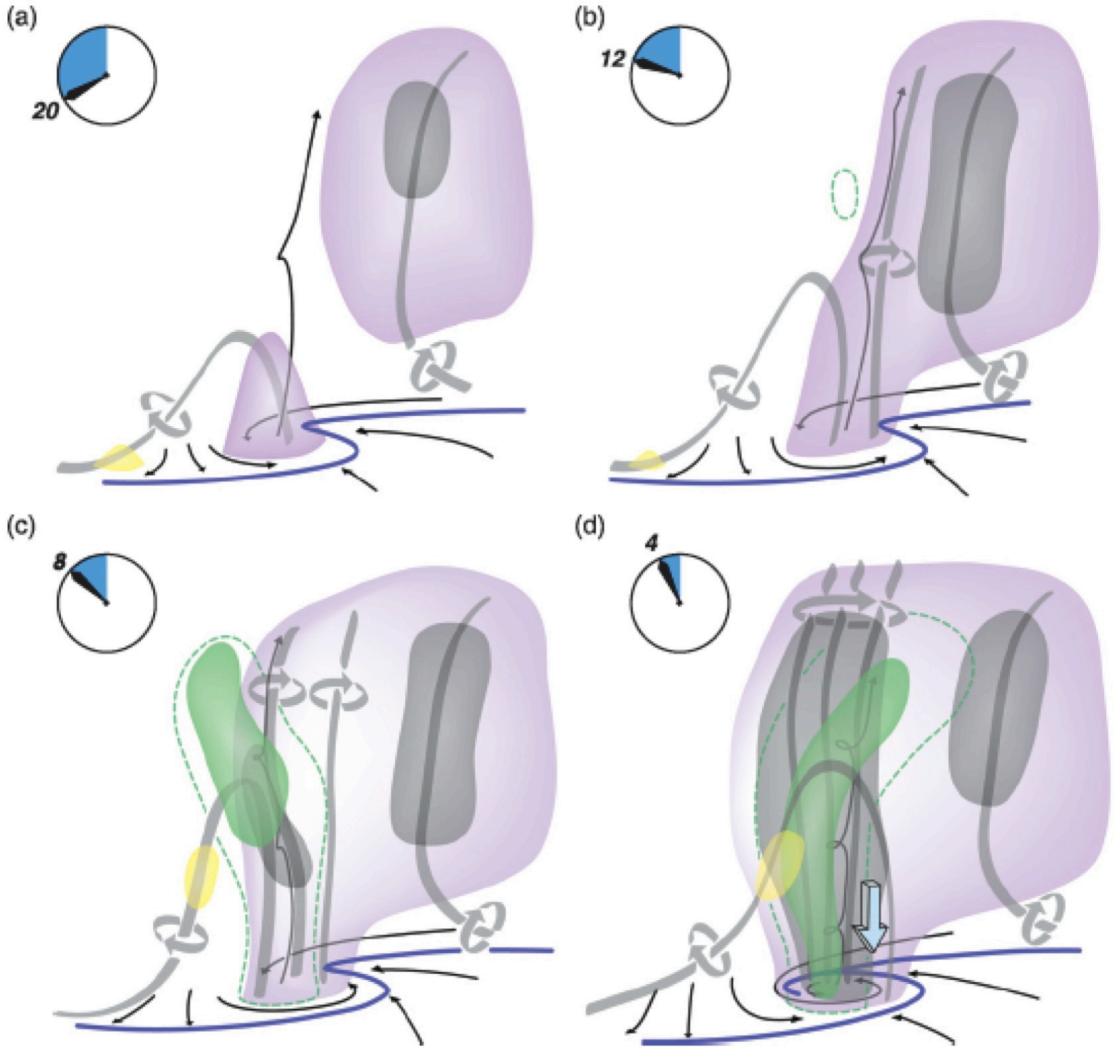

Figure 1.2: A conceptual schematic summarizing the pre-tornadogenesis dynamics associated with the Goshen County, Wyoming tornado-producing supercell observed by the VORTEX2 field campaign. This figure was taken from one of the campaign's resulting papers by Markowski et al. (2012a) and shows the pre-tornadogenesis environment (a) 20 min, (b) 12 min, (c) 8 min and (d) 4 min prior to tornadogenesis. Grey arrows indicate vortex lines. Yellow and purple isosurfaces indicate strong cyclonic and anticyclonic vertical vorticity, respectively. Grey isosurfaces indicate regions of stronger vertical cyclonic vorticity than the regions shaded in purple. Green isosurfaces show regions of larger-than-background reflectivity. Blue lines at the surface show surface gust fronts and black lines show surface streamlines. Notice the arched orientation of the vortex line originating near the rear gust front behind the blue line in (a). As the storm evolves, this vortex line is drawn vertically into the strong vertical cyclonic vorticity situated above associated with the storm's mesocyclone.

Chapter 2 – Methodology

The UW Non-hydrostatic Modeling System (NMS) was used to perform every simulation experiment in this thesis. The NMS is a compressible, non-hydrostatic atmospheric model with a 2-moment bulk microphysics scheme and 1.5-level turbulence closure using a three-dimensional Cartesian coordinate (Tripoli and Smith, 2014a,b). NMS is unique among cloud models in that it uses a fully three-dimensional Lamb vector based dynamical formulation designed to optimally capture the three-dimensional dynamical balances between the wind field and pressure. Moreover, finite differencing techniques originally developed by Arakawa and Lamb (1981) are extended to three dimensions in order to constrain the system against non-physical enstrophy production, resulting from truncation error. This uniquely equips the NMS to simulate fully three-dimensional vortex evolution including tumbling, twisting, and braiding of vortex tubes, all of which have been found to be of key importance during tornadogenesis in our simulations.

The NMS is employed to perform three distinct numerical experiments, each with their own individual devotion[1]. The first is a nested grid, full-physics, fully three-dimensional simulation of an idealized tornadic supercell used to expose the pre-tornadogenesis dynamics of the low-level environment. The results of this experiment prompt further investigation into the role of wind shear tilting by an isolated, negatively buoyant downdraft. Thus, the second simulation performed is actually a suite of supporting simulations of the simple dry dynamics of a downdraft plume subsiding

[1] Each simulation's unique setup is discussed at the beginning of each chapter dedicated to that simulation, or suite of simulations.

through a wind shear layer, independent of the full supercell environment. The third experiment performed is, again, a suite of simulations performed using the same model configuration as the idealized downdraft simulations. However, their design modifies specific aspects of the model configuration in order to expose the sensitivity of the downdraft experiment results to the subjectively chosen, simulated environment.

Chapter 3 – Idealized Tornadogenesis Simulation (NMS-Id)

This chapter presents the design and results of a nested grid, full-physics, three-dimensional numerical simulation of an idealized, tornado-producing supercell (hereafter referred to as the NMS-Id simulation, or the *idealized tornadogenesis simulation*). It first begins with an exposition on the simulation's unique model configuration.

a. Experimental Design

A three-dimensional simulation of a supercell resulting in tornadogenesis was performed using the thermodynamic and dynamic profiles and bubble initialization technique reported by Grasso and Cotton (1995). Dynamically, an f-plane at 35 degrees latitude was assumed, and the reference state flow was assumed to be in geostrophic balance although the reference-state thermal gradient associated with that balance was neglected. A Galilean transformation of the original Grasso and Cotton (1995) sounding was performed removing a mean west-southwest flow of 11 m s^{-1}. This produced a grid-relative southeasterly flow near the surface that veered with increasing height to a mainly westerly orientation around 3 km above ground level (AGL).

Four square-shaped nested grids of increasing spatial and temporal resolution were used to explicitly simulate the environmental interactions leading to tornadogenesis. The outer grid of 3 km spacing, spanning 300 km laterally, was used to simulate the meso-α scale environment of the storm over a sufficiently large region that the simulated supercell did not dramatically alter it over the 2.5 hour period of simulation. A vertical resolution of 120 m was used for the first 3 grids from the surface to 12.2 km AGL, where it was stretched to 600 m by 18.2 km, at which point the vertical spacing was kept constant to the

model top at 24.2 km AGL. A 7.2 km deep absorbing layer was applied as an upper boundary condition. 600 m horizontal spacing was used on the second grid spanning a horizontal distance of 72.5 km, which was sufficient to capture the basic meso-β scale supercell dynamical structure. Initial tests showed that the mesocyclone, together with a crude tornadic vortex, was captured even on this coarse resolution grid. A horizontal grid spacing of 120 m was used on the 3rd grid spanning a horizontal distance of 36 km. Hence, the vertical resolution and horizontal resolution was equal to 12.2 km AGL on the third grid, which was sufficient to crudely capture the misoscale tornadogenesis dynamics. To more competently capture the misoscale tornadogenesis dynamics, a 4th grid of 40 m spacing spanning 12 km was centered over the rear and forward flanking gust front intersection (or *cusp*) just before a tornadic vortex formed in the 3 grid simulation during preliminary tests. A vertical nest was also applied to the 4th grid to increase its vertical resolution to 40 m and match the horizontal resolution up to 1.2 km AGL. Vertical nesting was implemented by simply dividing individual grid cells into 3 equal layers and then using the usual nesting techniques across the 3rd to 4th grid vertical interface. Initially the nests were programmed to follow the expected location of the tornado determined by preliminary tests. Once the surface tornado vortex formed, the 3rd and 4th grids were programmed to center on and follow the lowest surface pressure simulated on the 4th grid.

The NMS radiation parameterization was not used and two-moment bulk microphysics were employed simulating cloud water, rain, pristine ice, soft graupel, hard graupel and aggregated crystals. A soil /vegetation parameterization was not used and, in its place, surface heat and moisture fluxes were set to zero. Surface friction was prescribed

using the Louis (1979) surface layer parameterization and a surface roughness height of 10^{-2} m .

The model was initiated with an elliptical warm thermal 10 km in horizontal diameter, 3 km in vertical diameter and centered 1.6 km AGL. The potential temperature anomaly across the thermal was specified with the function:

$$R = \sqrt{\left(\frac{x - x_0}{h_x}\right)^2 + \left(\frac{y - y_0}{h_y}\right)^2 + \left(\frac{z - z_0}{h_z}\right)^2} \tag{1}$$

$$\theta' = \begin{cases} A\cos^2\left(\frac{\pi}{2}R\right) & R \le 1 \\ 0 & R > 1 \end{cases} \tag{2}$$

where A is the bubble amplitude, R is the wavelength , and h_x, h_y and h_z are the thermal perturbation half-widths and x_0, y_0 and z_0 represent the Cartesian x, y and z components of the thermal perturbation center point. For the initial perturbation, $h_x = h_y = 5$ km; $h_z = 1.5$ km; A = 4 K.

An initial supercell, comprised of the bubble thermal formed an initial tornado-like vortex by 1500 s as the first precipitation reached the surface, but this chapter's analysis begins at 3000 s, when a secondary disturbance formed, which was less dependent on the initial bubble forcing.

b. Results

Figure 3.1a depicts a newly formed density current where the term *density current* is meant to represent a surface-based, propagating, relatively dense, divergent pool of air forced by the downward mass flux of cool air from a precipitation-driven downdraft. Its existence is marked by the horizontal equivalent potential temperature gradient (θ_e) at the surface and via the vertical cross section of θ_e in Figure 3.1a, which serves to provide a sense of the density current's three-dimensional spatial structure.

i. Arching Vortex Sheet

The first noticeable aspect of this environment is the presence of a vortex sheet that bent over and imitated the geometric shape of the density current with cyclonic vertical vorticity along its leading, or eastward, edge extending all the way to the ground (Fig. 3.1b). This leading edge interface with the low-level environment will also be referred to as the storm's Rear Flanking Gust Front (RFGF). Notice that, once an increased value of vorticity is rendered as an isosurface, the vortex sheet appeared considerably more arched immediately along the RFGF (Fig. 3.1c). This is indicative of the density current leading head's circulation underneath the vortex sheet that the sheet is subsequently arched/bent over. This assertion will be further verified in Chapter 5, but the shape of the vortex sheet will manifest itself in the orientation of developing vortex tubes later in this simulation's evolution. It is, therefore, important to call attention to. Investigating the contribution of vertical vorticity to the total vorticity along the RFGF revealed that positive vertical vorticity was more than 6 times stronger than the horizontal vorticity magnitude immediately along the gust front (Fig. 3.1d). This indicates that, although baroclinically

produced vorticity inevitably existed, the horizontal shear across the RFGF was of large enough magnitude to significantly contribute to the total vorticity magnitude seen there.

ii. Vortex Sheet Roll-Up Process

Since, by nature, vortex sheets are inviscidly unstable (Wu et al. 2006), disturbances of any wavelength will amplify at the expense of the surrounding, background kinetic energy and the vortex sheet will deform and break down (Batchelor 1967) if the growth tendency exceeds whatever viscous damping exists. The result of such a break down is the *vortex sheet roll-up process* (Drazin and Howard 1966; see Chapter 1d) that has been associated with the development of dust devils, gustnadoes and relatively weak, short-lived tornadoes in non-supercell thunderstorms (e.g. Barcilon and Drazin 1972; Bluestein 1980; Bluestein 1985; Wakimoto and Wilson 1989; Lee and Wilhelmson 1997a,b; Marquis et al. 2007). Four minutes further into the idealized tornadogenesis simulation, the same process appeared to be occurring along the RFGF where vertically oriented vortex tubes, situated along the RFGF, looked bent back over the cold pool in the same way the original vortex sheet was arched (Fig. 3.2a).

Figure 3.2c shows low-level vertical vorticity associated with the RFGF. Looking specifically at the region highlighted by the white circle, the center of the vortex sheet roll-up was bound by zero-lines in the vertical vorticity field indicating that an inflection point and necessary condition for a shearing instability (Rayleigh 1880) existed along the outflow boundary where the roll-up was taking place. A time series is also provided in Figure 3.2d to explicitly show the growth of the inflection point at the center of the instability 3200 s into the simulation, only 50 s prior to the images shown in (a), (b) and

(c). This growth suggests that the vortex tube associated with this same region in Figure 3.2a was the result of a shearing, barotropic instability, which is manifested in the streamlines of Figure 3.2b as well. Through closer inspection, it can be seen that the vortex tube in Figure 3.2a was only partially rolled-up, confirming the role of a roll-up process to the tube's origin.

iii. Low-Level Vertical Vorticity Intensification

Note that the partially rolled-up vortex tube was arched considerably in the vertical direction, roughly 1.5 km. Although not explicitly shown in Figure 3.2, additional investigation revealed that the mesocyclone updraft and arched tube were approximately co-located, perhaps not by accident. Therefore, in addition to the vertical motion forced on the edge of the outflow by the density current leading head's circulation, vortex stretching by the storm's low-level inflow triggered an aggregation process by which surrounding vorticity was brought into the circulation of this original arched vortex tube. Via calculation of a quantity related to swirl ratio (e.g. Davies-Jones 1973; see Eq. 1.2), one can quantify whether, or not, the vorticity truly was experiencing intensification due to vertical stretching. This quantity, calculated as, $w \cdot \left(\partial v / \partial x - \partial u / \partial y \right)$ represents the vertical stretching of surface-based vertically oriented vorticity since flow vanishes at the ground. Figure 3.3 shows this stretching quantity by a vertical cross section that penetrates the center of the instability and vortex tube in Figure 3.2. Along the RFGF, this quantity was maximized at the core of the vortex sheet instability indicating that the resulting vortex tube was in fact being stretched vertically. Thus, convergence at its base was enhanced

and surrounding vorticity was aggregated into its circulation, ultimately intensifying the vortex.

Stretching of the arched vortex tube can be seen in Figure 3.4 where the white arrow indicates the vortex arch's summit and region closest to the base of the mesocyclone. At this point, roughly 4 min further into the simulation from Figure 3.2, what was once an arched, partially rolled-up vortex tube (Fig. 3.2a), strengthened and stretched into a cyclonically rotating vortex tube that still bent back over the cold pool (Fig. 3.4). Notice there was relatively little of the vortex sheet remaining along the RFGF, exhibiting its aggregation into the circulation of the stretching vortex tube.

Finally, after nearly twelve minutes of the vortex sheet roll-up process and subsequent vertical stretching, a tornadic vortex was visibly extending from the mesocyclone's mid-level (1-3 km AGL) vorticity to the surface (Fig. 3.5). Although there was still baroclinicity associated with the cold pool in the low-level environment (evident by the surface-θ_e), there was little significant vertical vorticity along the RFGF. This suggests the vortex was largely dependent on its connection with the mid-level vorticity of the mesocyclone for further maintenance.

c. Discussion

Tornadogenesis in the NMS-Id simulation was preceded by a vortex sheet roll-up process along the storm's rear flanking cold outflow boundary, or RFGF. This agrees with the dated hypothesis of Bluestein et al. (2003). However, a significant feature of the roll-up process not theorized by Bluestein et al. (2003) is that resulting vortex tubes arched over the cold pool with cyclonic vertical vorticity along the RFGF extending all the way to

the ground. Given the recent body of research highlighting the existence of vortex lines that originate and arch in a similar manner prior to tornadogenesis (M08; Marquis et al. 2012; Markowski et al. 2012a), it is encouraging to see that the low-level kinematic environment produced by the roll-up process is in agreement with current literature and observations.

From analysis of alternative preliminary numerical simulations of tornadic supercells, it is has become increasingly obvious that roll-up initiation tends to originate in a specific region along the RFGF. That is, downstream of the RFGF and Forward Flanking Gust Front (FFGF) cusp, directly beneath the base of the mesocyclone aloft. This is also the same location where misovortices tend to intensify, leading to tornadogenesis (Fig. 3.4). It is here that the vertical motion of the density current leading head's circulation is likely connected into the primary supercell updraft where sustained vertical motion intensifies the low-level vorticity through vertical stretching. The effect is to then either initiate a vortex sheet roll-up process, or stand up existing misovortices and direct them into the primary updraft stream and dynamic pressure field of the mesocyclone aloft, dramatically decreasing the swirl ratio (e.g. Davies-Jones 1973; see Eq. 1.2) and promoting upscale vertical vorticity growth toward full tornadogenesis. This analysis may consequently provide a conceptual justification for the dynamic pipe effect (DPE) theory, or at least demonstrate how the mesocyclone's dynamic pressure field is involved in the extension of its vorticity to the surface.

Interestingly, the aforementioned process benefits from the low-level Storm Relative Helicity (SRH) characteristic of the environment as well. An environment with

strong, positive, low-level SRH may aid the upscale growth and maintenance of developing vortex tubes along the vortex sheet because the mesocyclone's upper level divergence is necessary to sustain the developing vortex tube's vertical motion. Vertical motion that extends through the developing vortex tube along the RFGF and upward into the mesocyclone updraft is supported by the low-level positive SRH, which establishes a streamwise circulation into the vortex tube from below and out of the vortex tube above. This implies that the low-level SRH may be the low-level environmental characteristic responsible for the upscale growth of vorticity along the RFGF, specifically near the rear and forward flanking gust front cusp. This may also help explain the importance of 0-1 km SRH to tornadic supercells (Markowski et al. 2003).

Analysis of this chapter's results suggests that the observed low-level vortex features are derived from the vortex sheet formed along the RFGF as a consequence of ambient horizontal vorticity and SRH tilting by a precipitation-laden downdraft. Vortex line arching theory (see S07; M08) alternatively attributes the same kinematic environment to the bending of vortex lines associated with the downdraft's baroclinically generated vorticity by an updraft-downdraft interaction. Yet, the results presented here suggest that the mechanism responsible for these vortex features does not exclusively involve the baroclinic vorticity of the RFD. Instead they rely on the downdraft's downward momentum transport that directly results in a vertically oriented and barotropically unstable sheet of vertical vorticity bending over the leading head of the RFD's associated density current. Therefore, this may indicate that a downdraft's role in the pre-tornadogenesis dynamics of a supercell storm may involve wind shear and helicity tilting

more than currently thought. This analysis may then serve as a preliminary confirmation of this thesis' hypothesis.

However, if this hypothesis were true, one would expect that such a process could be replicated in a simple model that excludes the complexities of a supercell environment. If the strength of sheet's vorticity is entirely derived from the ambient low-level wind shear, then prescribing a cold bubble to subside in a vertically sheared environment should result in a low-level kinematic environment comparable to that of the NMS-Id simulation. Additionally, this simple model's low-level dynamical evolution should manifest a relationship between resulting RFGF vortex features and the SRH characteristic of the prescribed environment. It is, therefore, mandatory that such experiments be performed in order to justify the statement that a downdraft's subsidence through low-level vertical wind shear can explain the dynamics precursory to tornadogenesis in the NMS-Id supercell simulation. The design and results of these experiments are discussed in the following chapter after a more detailed discussion of their theoretically expected outcomes is given.

Chapter 3 Figures

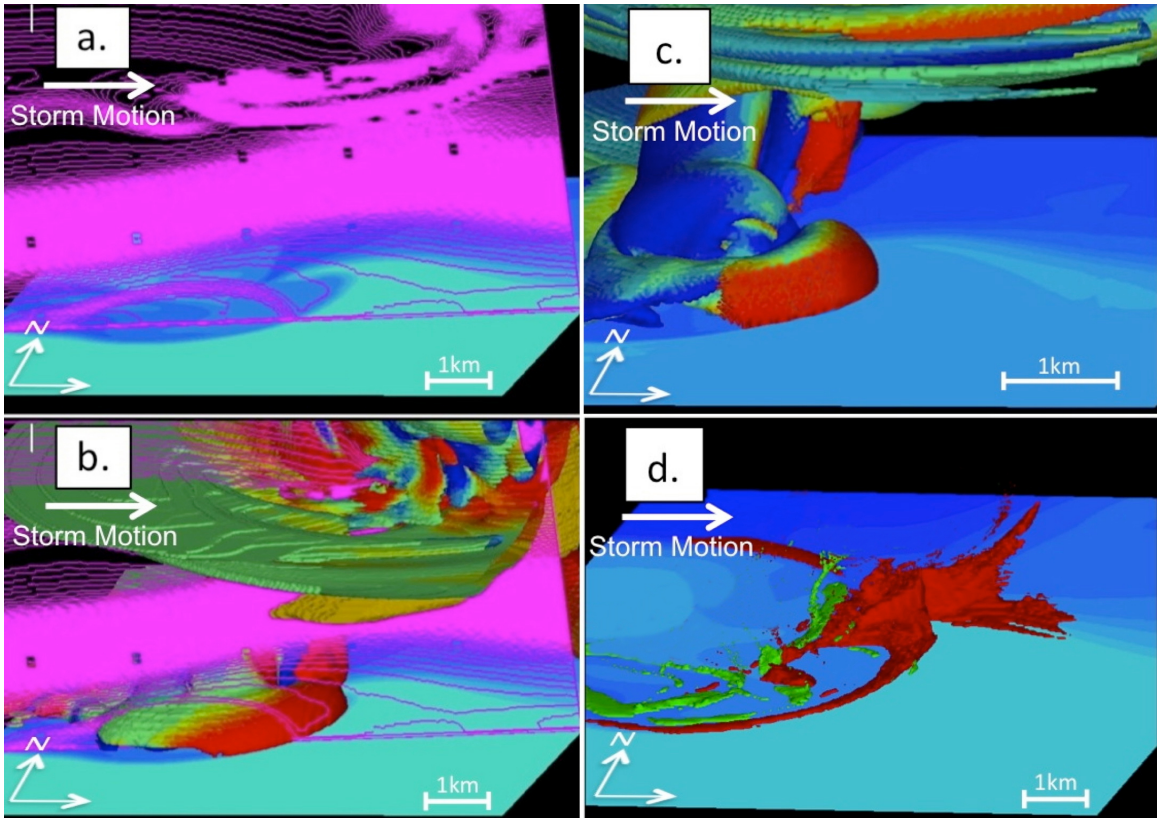

Figure 3.1: An oblique view from the South-Southeast of the idealized supercell's density current, 3000 s into the NMS-Id simulation. In all of the images, the colored horizontal cross section shows ground-level equivalent potential temperature, θ_e (*light blue*: warmer, *dark blue:* cooler). (a) A vertical cross section of equivalent potential temperature contoured every .1 K that serves to provide a three-dimensional perspective of the density current seen in the surface-θ_e horizontal cross-section (magenta contours). (b) The same as (a) with the addition of a three-dimensional isosurface representing the magnitude of three-dimensional vorticity with a value of .02 s^{-1}. This isosurface is colored by the sign of the total vorticity's vertical component (*red:* cyclonic, *blue*: anticyclonic, *green-yellow*: primarily horizontal). (c) A three-dimensional isosurface of total vorticity magnitude colored the same as (b), but the isosurface value is increased to .05 s^{-1}. (d) A three-dimensional isosurface representing the ratio of vertical vorticity (*red:* positive, *green:* negative) to horizontal vorticity magnitude of a value greater than, or equal to, 6.

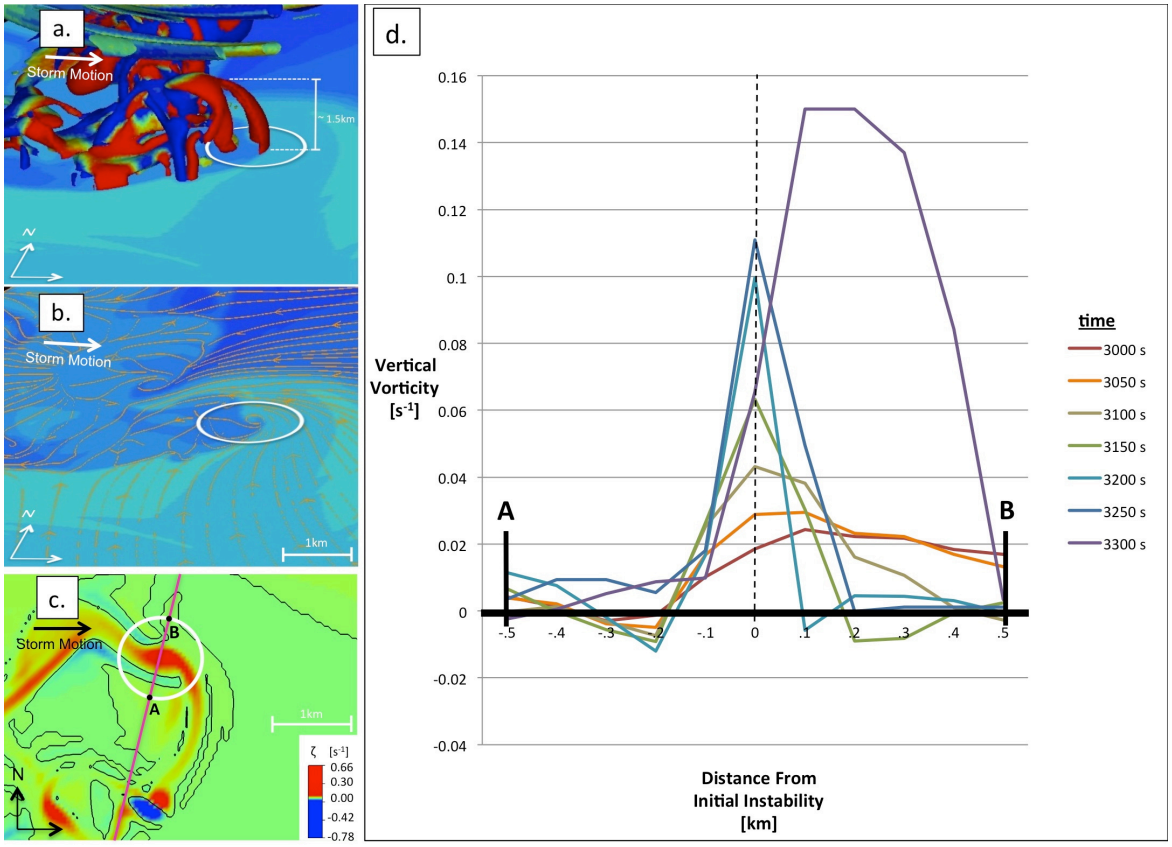

Figure 3.2: The observed RFGF vortex sheet roll-up process's initiation as described in Section 2.2. (a), (b) and (c) show the NMS-Id simulation 3250 s after model initiation. (a) A three-dimensional isosurface of total vorticity magnitude equal to .05 s^{-1} colored the same as Figure 1b viewed from the South. The white oval is used to draw attention to the partially rolled-up, arched vortex tube it encircles while the vertical scale bar gives perspective of the height of the arched tube, roughly 1.5 km. (b) Same as (a) with the total vorticity isosurface removed. The orange, near-surface streamlines provide a visualization of the horizontal shear instability along the RFGF roughly 100 m from the ground. (c) A top-down view of the RFGF and the associated 100 m AGL vertical vorticity field colored as in Figure 3.1b. The white circle encompasses the same arched tube in (a) and (b). Black lines indicate contours of zero vertical vorticity. (d) A time series of vertical vorticity along the magenta line indicated in (c) between points A and B from 3000-3300 s into the NMS-Id simulation. The center of the tube in (c) is the center of the instability in (d).

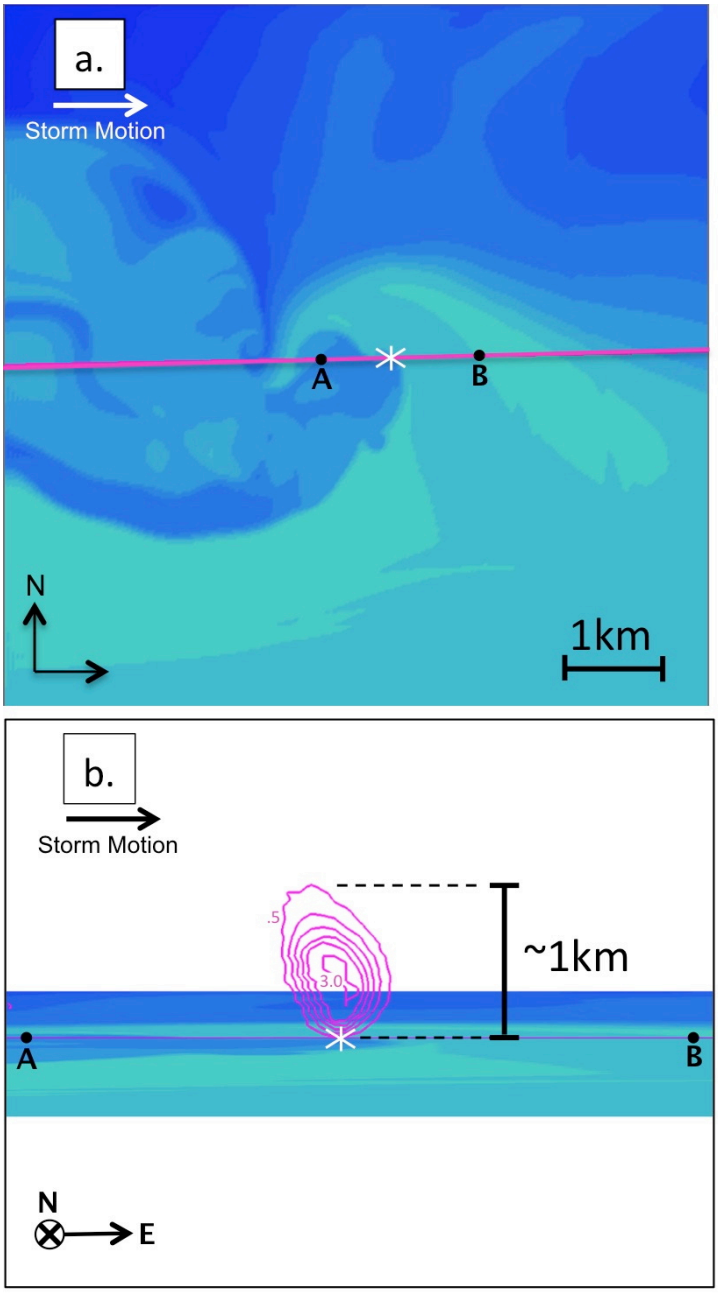

Figure 3.3: Vertical cross section through the instability along the RFGF at the same simulation time as Figure 2. The cross section shows a quantity calculated as $w \cdot \left(\partial v/\partial x - \partial u/\partial y\right)$, which is the vertical stretching of surface-based, vertically oriented vorticity since vertical motion is zero at the surface. (a) Looking down at the surface-level equivalent potential temperature colored as in Figure 3.1a, the magenta line shows the orientation of the cross section. (b) The vertical stretching quantity cross section as viewed from the South. Magenta contours show lines of constant vertical stretching quantity at .5 m s^{-2} intervals to manifest an area of maximum stretching through the instability. The core of this quantity's maximum shown in (b) is > 3.0 m s^{-2} and its height is roughly 1.5 km.

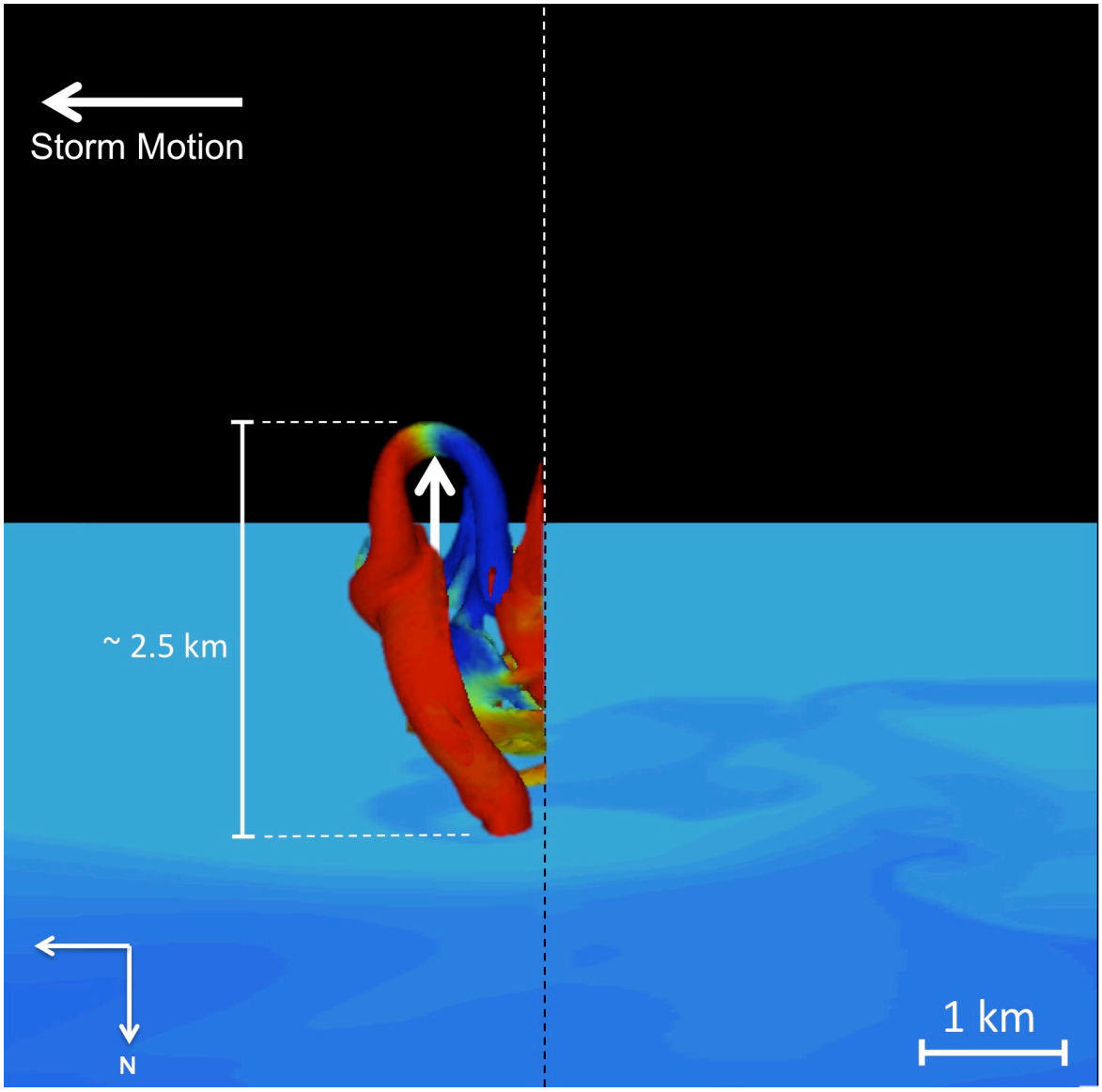

Figure 3.4: An oblique view from the North of the arched vortex tube while being stretched vertically as a result of the arched vortex tube's interaction with the supercell's updraft 3400 s after model initiation. To cleanly view the vortex tube as it was stretched vertically, rendered total vorticity isosurfaces west of the vortex tube were clipped out of the image. The dotted line in the center of the image shows from what point the image was clipped. The horizontal cross section is the same as in Figure 3.1 and the three-dimensional isosurface is the same as in Figure 3.2a. The white arrow is used to indicate the region of stretching by the updraft. Measured vertical vorticity values at the core of the funnel were .24 s^{-1}.

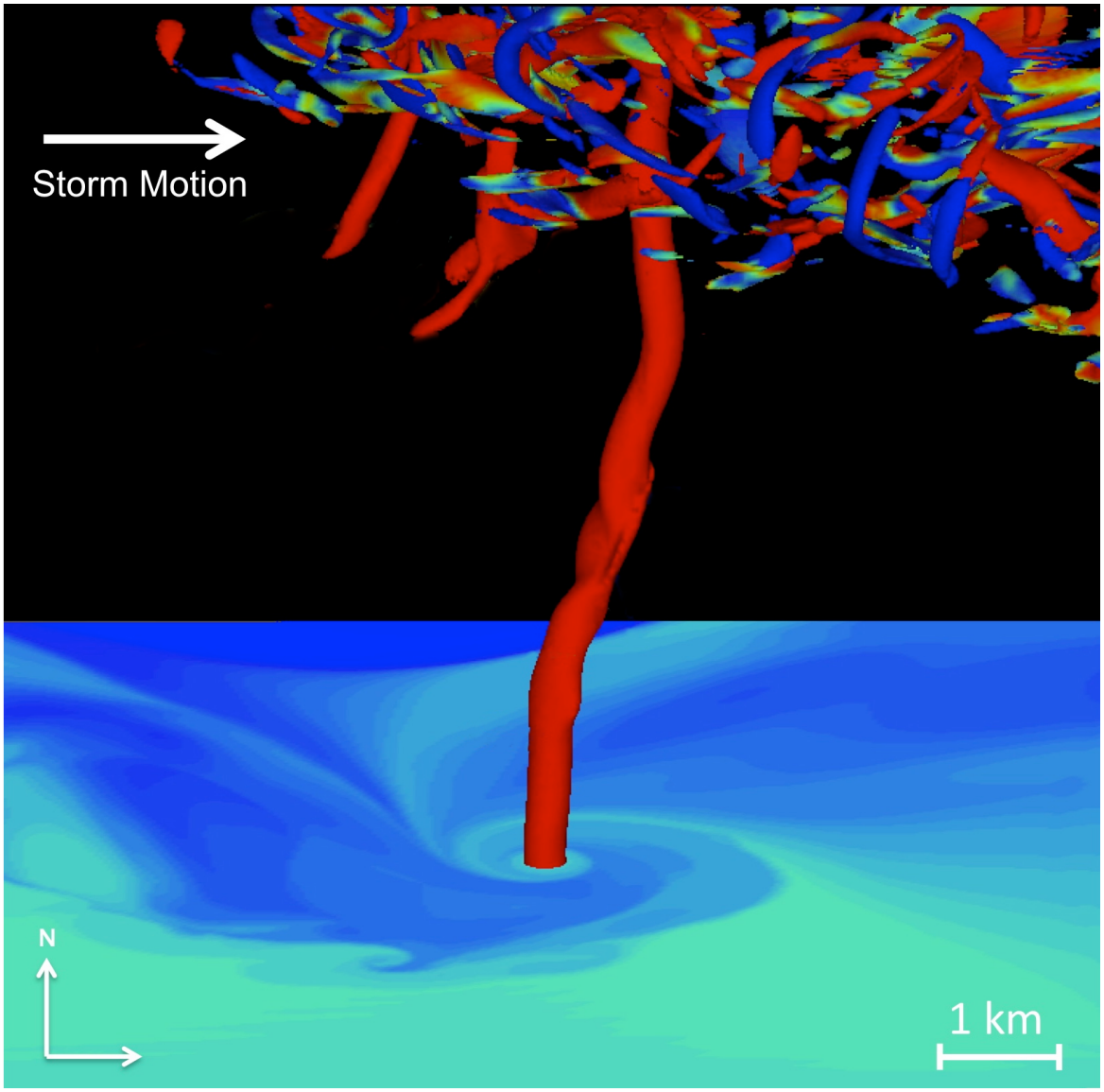

Figure 3.5: An oblique view from the South of a mature vortex funnel 4200 s into the NMS-Id simulation. The horizontal cross section is as Figure 3.1 and the three-dimensional isosurface shows a three-dimensional vorticity magnitude equal to 2.5 s^{-1}, colored as in Figure 3.1b. Core vertical vorticity inside the vortex was found to be approximately .6 s^{-1}.

Chapter 4: Idealized Downdraft Simulations

This chapter discusses the design and results of a suite of simulations performed in a highly idealized environment in order to expose the low-level vorticity evolution specifically attributable to wind shear and helicity tilting by a downdraft. Before the experimental design is discussed, key theoretical features of these experiments are emphasized. The discussion of these features, complete with a schematic of the anticipated relationship between model-prescribed vertical wind shear and resulting low-level vorticity, begins below.

a. Theory

If downdraft-induced wind shear tilting is responsible for the RFGF vortex sheet in the NMS-Id simulation, the strength of the sheet's vorticity is then entirely derived from the strength of the ambient, low-level horizontal vorticity. This, in addition to the baroclinicity of the propagating cold pool, also manifests itself in the magnitude of convergence along the RFGF. Since barotropic instabilities along a vortex sheet require the necessary condition of an inflection point in the kinematic field, convergence along this boundary could initially determine the size of growing barotropic instabilities by limiting the width of what Lee and Wilhelmson (1997a) define as a transition zone between the two fluids with markedly different speeds. It is the width of this transition zone that determines the spatial extent of the inflection point in the horizontal flow and consequently the initial size of developing barotropic instabilities in the preliminary stages of the vortex sheet roll-up process. While this conceptualization may explain why tornadogenesis is sensitive to the strength of the cold pool's baroclinicity and low-level environmental vertical wind

shear (e.g. Thompson et al. 2003; Craven and Brooks 2004), it also provides a theoretical basis for the anticipated relationship between model-prescribed vertical wind shear and the resulting low-level kinematic features of this chapter's highly idealized downdraft experiments.

Furthermore, the growth and maintenance of developing instabilities along the gust front is only favored when the low-level environment has the added characteristic of positive SRH. This is because, without adequate vertical motion through developing instabilities as a consequence of negligible SRH, instabilities will develop a dynamic pressure field and draw air into themselves from all sides. This eliminates the possibility of achieving cyclostrophic balance with any significant circulation. When the growth of instabilities are stunted in this way, they cannot benefit from the aggregation of surrounding vorticity either. The effect of low-level SRH is to then support the growth of outflow boundary instabilities by establishing streamwise circulations through developing vortices and to help them maintain cyclostrophic balance with appreciable vorticity. It is then expected that a model-prescribed, low-level environment characterized by a straight-line hodograph (no SRH) will result in numerous outflow boundary instabilities when a cold bubble falls through the environment to the surface, because none of the instabilities will grow through aggregation of surrounding vorticity. Alternatively, in an environment prescribed with a wind shear profile characterized by a clockwise-curved hodograph (positive SRH), convergence along the surface outflow's leading boundary is weakened relative to the straight-line hodograph case. Upward motion through the outflow

boundary's vortex sheet then supports the growth and maintenance of larger, more robust vortex features that are far less numerous along the outflow boundary.

Consolidating these assertions yields a theoretical basis for the idealized downdraft experiments in this chapter. If downdraft-induced wind shear and helicity tilting is largely responsible for the low-level dynamical evolution in the NMS-Id simulation, the results of experiments that simulate the dry descent of a downdraft through a low-level wind shear layer should show the following. An isolated downdraft subsiding into a low-level wind shear layer characterized by a straight-line hodograph should result in a surface outflow boundary vortex sheet that becomes rapidly decomposed into small and numerous vortex tubes (Fig. 4.1a). An isolated downdraft subsiding into a low-level wind shear layer characterized by a clockwise-curved hodograph should result in a surface outflow boundary vortex sheet that remains relatively well composed, but breaks down into more robust and fewer vortex tubes (Fig. 4.1b). Figure 4 graphically illustrates this relationship and the expected results of the idealized downdraft experiments. The design of these experiments is discussed in the next section.

b. Experimental Design

Embedded within a horizontally homogeneous domain, a potential temperature perturbation with negative buoyancy was placed immediately above a shear layer, pre-defined by a sounding composed of an idealized vertical wind shear profile in three simulations. Equivalent to previous work investigating the evolution and dynamics of cold outflow in numerical simulations (e.g. Mitchell and Hovermale 1977; Lee and Wilhelmson 1997a; Orf and Anderson 1999) each simulation was run without moist physics in order to

isolate the dry dynamical processes of the downdraft/environment contributing to the formation of the surface vortex sheet.

Each experiment was conducted with a different initial vertical wind shear profile. The hodographs associated with these profiles can be seen in Figure 4.2. The first was used to define a control environment for comparison where, throughout the entire depth of the simulated domain, horizontal and vertical wind speeds were set equal to zero (Fig. 4.2a). The second vertical wind shear profile represented a linear, unidirectionally sheared environment within the first 1 km depth of the domain. This unidirectional shear was oriented east-west, with mid-level westerly flow speeds set to 10 m s^{-1} that decayed linearly below 1 km to a value of 0 m s^{-1} at the surface (Fig. 4.2b). To inhibit the thermal perturbation's migration out of the domain, a Galilean transformation was applied to the grid by removing a mean westerly wind of 10 m s^{-1}. This transformation is specific to this simulation and is represented on the hodograph in Figure 4.2b by the symbol, "G". The third and final wind shear profile was defined to initialize the model environment with a profile recognized as favorable for tornadogenesis (Weisman and Klemp 1981). That is, relatively light (~5 m s^{-1}) and southerly winds near the surface that intensified and veered with increasing height to roughly 1 km above the surface. Here the flow remained westerly with a speed of roughly 12 m s^{-1} throughout the rest of the vertical domain to produce a strongly clockwise-curved hodograph (Fig. 4.2c). To again inhibit the thermal perturbation from migrating out of the simulation domain, a Galilean transformation was applied to the grid by removing a mean southwesterly wind of 7 m s^{-1}. Again, this

transformation is specific to this simulation and is represented on the hodograph corresponding to this vertical wind shear profile by the symbol, "G", in Figure 4.2c.

The potential temperature perturbation, or cooling function, used to parameterize the downdraft was initiated just above (within 500 m) the top of the specified shear layer and had the fundamental form given by (1) and (2) in Chapter 3a, but where t = time and $A = g(t)$. The temporal function $g(t)$ represents the cooling rate amplitude and was specified such that it increased from 0 to 0.01 K s^{-1} over the first 11 min of the simulation. For a remaining 5 min, $g(t)$ stayed at a constant value of 0.01 K s^{-1} until completely turning off 16 min into the simulation and reaching a minimum potential temperature perturbation value of ~ -4 K. The potential temperature perturbation was designed to emulate the spatial specifications of the parameterization used in Orf and Anderson (1999). Therefore, $h_x = h_y$ = 1200 m; h_z = 1800 m and the resulting geometric shape of the perturbation was that of a prolate ellipsoid.

Each simulation used a square-shaped horizontal domain of 144 km^2 to a height of 4 km with horizontal and vertical resolutions of 60 m. Each simulation also used a large time step of 1 s and neglected surface friction to allow a free-slip lower boundary. The influence of Earth's rotation and curvature were neglected to eliminate geostrophic adjustment processes influencing the results.

Finally, in the interest of clarity, each of the simulations was given a name that represented the vertical wind shear profile used in combination with the ellipsoid cooling function that was common to all three simulations. Therefore, "No-Shear-Ellipsoid" (NS-E) identifies the simulation initialized with a completely static environment,

"Unidirectional-Shear-Ellipsoid" (US-E) identifies the simulation using the wind shear profile seen in Figure 4.2b, and "Directional-Shear-Ellipsoid" (DS-E) identifies the simulation using the vertical wind shear profile in Figure 4.2c. The results of these experiments are discussed in the following section.

c. Results

i. Thermal Field Evolution

Figure 4.3 shows the results of the idealized downdraft simulations in the form of a -0.1 K potential temperature perturbation, three-dimensional isosurface. One of the most obvious aspects of this sequence of images is that, once the downdraft reached the surface, cold outflow propagated in all directions as a density current. This cold outflow density current's leading (eastward) edge stood taller than the upstream (westward) edge when the domain was specified with a vertical wind shear (Fig. 4.3b and 4.3c) as a result of its upstream propagation relative to the low-level environmental flow.

Prior to the downdraft reaching the surface, relatively cold, dense air fell at an angle relative to the ground when vertical wind shear was added (Fig. 4.3b and 4.3c), with some of the less-negatively buoyant air suspended at an elevation comparable to the perturbation's initialized vertical height. This is evident in the US-E (Fig. 4.3b) and DS-E (Fig. 4.3c) simulations after 15 min of model evolution. Interestingly at this time, the shape of the evolved thermal perturbation field above the surface took the form of an elongated arch that stretched in the direction of the mid-level winds. As the simulation

evolved, this arch shape dissipated in both simulations, which is likely indicative of turbulent entrainment along the edges of the thermal perturbation.

ii. Dynamics Evolution

The first 9 min of each simulation showed similar characteristics in the evolution of both their vorticity and thermal perturbation fields (Fig. 4.3). However, adding a vertical wind shear profile in the US-E (Fig. 4.4b) and DS-E (Fig. 4.4c) simulations revealed that, as the cold downdraft subsided, its northern side experienced vertically oriented cyclonic rotation while its southern side experienced vertically oriented anticyclonic rotation. This distribution of vorticity was only observed to maintain itself in the simulation with a directionally sheared vertical wind profile. In addition, as the vorticity field of the DS-E simulation (Fig. 4.4c) evolved, vorticity in the form of an elongated, towering vortex arch appeared to stretch vertically in the same way that the thermal perturbation field arched (Fig. 4.3c). This arch was of appreciable size (roughly 1 km in diameter) and extended roughly 1.5 km in the vertical, equivalent to the initialization height of the thermal perturbation. The maximum vertical vorticity magnitude associated with the cyclonic (shaded red) branch of the towering vortex arch was nearly .6 s^{-1} roughly 500 m from the ground.

A vortex sheet characterized by positive vertical vorticity along the surface outflow boundary was also seen in the idealized downdraft simulations prescribed with non-zero vertical wind shear (Fig. 4.4b, 4.4c). By the oppositely signed vertical vorticity values on its upshear (western) and downshear (eastern) sides, the vortex sheet in the DS-E simulation appeared arched over the outflow boundary to a height of around 500m. Figure

4.5 provides an alternate viewing perspective to visualize this region of the domain more clearly, and also shows a smaller value of three-dimensional vorticity magnitude (.02 s^{-1}) to observe potentially smaller scale vortex features. Looking from the northeast, the magnitude of vertical vorticity in the US-E simulation (Fig. 4.5a) was nearly triple that of the DS-E simulation (Fig. 4.5b). In addition, these sheets of vorticity appeared to roll-up into vortex tubes along the outflow boundary while also maintaining the arched shape of the original vortex sheet. The resulting size and concentration of these vortex tubes along the US-E and DS-E simulation outflow boundaries appeared correlated with the low-level vertical wind shear prescribed. That is, when a straight-line hodograph was used in the US-E simulation, numerous small and intense vortex tubes lined the outflow boundary. When a clockwise-curved hodograph was used in the DS-E simulation, resulting vortex tubes were far less numerous, were of larger size and were located on the northeastern edge of the outflow boundary.

Associated with the towering, vertically elongated vortex arch in the DS-E simulation, a couplet of cyclonic and anticyclonic vorticity was observed at low-levels (roughly 300 m AGL) and straddled the surface cold pool (Fig. 4.6). These counter-rotating vortices were also seen in the US-E simulation, although their circulations were far less notable compared to those of the DS-E simulation. Figure 4.6 also serves to provide an additional perspective of the outflow boundary vortex sheet's evolution in both the US-E and DS-E simulations. When the thermal perturbation was embedded in a directionally sheared environment, a sheet of vorticity along the density current's leading,

northeastern edge was clearly seen 13 min into the simulation (Fig. 4.6b). As the simulation evolved 6 min further, this sheet rolled-up into discrete and isolated vortices.

d. Discussion

Vortex sheets were seen along the leading edge outflow boundaries of the idealized downdraft simulations with non-zero vertical wind shear profiles. In both the US-E and DS-E simulations, these vortex sheets appeared to arch over the outflow boundaries and eventually broke down, or rolled-up, into discrete and arched vortex tubes. Interestingly, the prescribed vertical wind shear appeared correlated with the vortex sheet's characteristics and evolution. To compare the results of these downdraft experiments to what was anticipated in Chapter 3a, Figure 4.7 shows the predicted and actual results of the idealized downdraft simulations together. When the prescribed low-level vertical wind shear was characterized by a straight-line hodograph, the transition zone along the outflow boundary was minimized. Consequent vortices along the front as a result of barotropic instabilities were, therefore, strong but small and numerous. When the prescribed low-level vertical wind shear was characterized by a clockwise-curved hodograph, the outflow boundary vortex sheet remained relatively well composed, but broke down into larger-scale, more robust vortex tubes along the northeastern edge of the outflow. These results are consistent with what was predicted and strongly indicate that the low-level, pre-tornadogenesis dynamics and kinematic features of the NMS-Id simulation were a result of vertical wind shear tilting by the storm's RFD.

It was the DS-E simulation that was most reminiscent of the RFGF evolution in the idealized tornadogenesis simulation discussed in Chapter 3. However, there were two

characteristics of the pre-tornadogenesis environment in Figures 3.1 through 3.4 that were not readily seen in the DS-E idealized downdraft simulation. First, the DS-E simulation's vortex sheet did not imitate the entire geometric shape of the density current as was seen in the NMS-Id simulation (compare Fig. 3.1b with Fig. 4.5b). Its arching was confined to the leading edge of the advancing cold pool, much like the idealized tornadogenesis simulation showed when the isosurface value of three-dimensional vorticity magnitude was increased (Fig. 3.1d). However, in agreement with the conclusions made for the shape of the vortex sheet seen in the NMS-Id simulation (Fig. 3.1b), the consistent arched nature of the vortex sheet in the DS-E simulation is evidence of the density current leading head's circulation. Second, the upscale growth of rolled-up vortex tubes was limited. This is likely because misovortices along the leading edge of the density current in the non-supercell environment of the DS-E simulation lacked sustained vertical motion throughout a deep layer. This is evident in Figure 4.8 where a cross section of the same vertical stretching quantity shown in Figure 3.3 is used for comparison through a vortex tube along the DS-E simulation's outflow boundary 27 min into the simulation. While the vertical vorticity values of both vortex features were comparable and the stretching quantity was maximized at the core of both features, vertical stretching in the DS-E simulation was one-third smaller than in the NMS-Id simulation (compare Fig. 3.3b and Fig. 4.8b). This indicates that vertical motion and stretching of the rolled-up vortex tube along the DS-E simulation gust front was weaker. Consequently, the tube's circulation was not as able to aggregate surrounding vorticity and the vortex features along the outflow boundary remained isolated from one another.

Via the arched vortex sheets and roll-up processes observed, this chapter's results showed that downdraft-induced wind shear and helicity tilting could explain some of the elementary features of the low-level pre-tornadogenesis environment in the NMS-Id simulation. Without the full supercell environment to benefit from, the most reminiscent low-level kinematic environment was produced when the model was initialized with a vertical wind-shear profile known to be favorable for tornadogenesis (Wesiman and Klemp 1981). This emphasizes a relationship between the RFGF roll-up process and low-level SRH that wasn't explicitly obvious in the NMS-Id simulation and that isn't explained in vortex line arching models of tornadogenesis. Additionally, this simple model also accounted for the low-level, counter-rotating vortices that are observed to straddle the cold pool of supercell thunderstorms (S07).

However, these results are a product of a highly idealized numerical environment initialized with numerous subjectively chosen domain specifications. In order to investigate how some of these specifications influenced the results, experiments were performed that tested the significance of the thermal perturbation's definition, the shear layer's depth and the surface friction parameterization used. These experiments are discussed in the next chapter.

Chapter 4 Figures

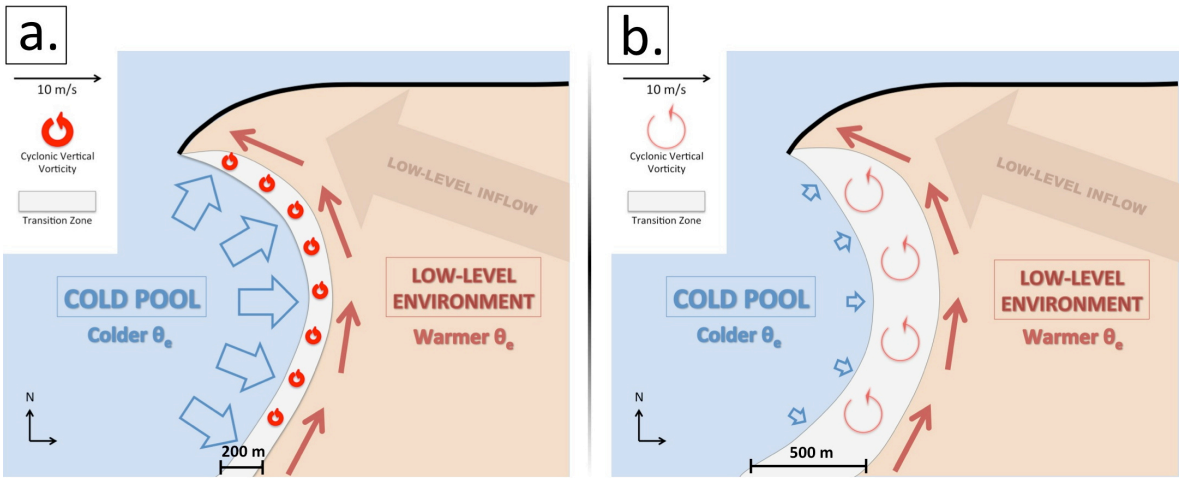

Figure 4.1: A graphical illustration of the anticipated relationship between vertically-oriented vorticity observed along the leading edge of an outflow boundary and vertical wind shear. In both illustrations, an idealized environment characterized by south-southeasterly low-level winds (brown arrow) and westerly mid-level winds is assumed. The westerly mid-level winds are brought to the surface by means of the RFD establishing the outflow boundary of interest. In addition, the outflow's momentum is illustrated using blue vectors (whose magnitudes can be determined via the provided scale at the top-left corner of each image). Vectors colored in red illustrate southerly gust-front-relative environmental winds. The gray area in each image indicates the RFGF transition zone between the westerly momentum of the cold outflow and the south-southeasterly momentum of the low-level environment. In each of the following cases, the change in wind shear is assumed to be a result of increasing the mid-level winds and not the low-level environmental wind, which remains fixed. (a) In the case of a low-level wind shear layer characterized by a *straight-line hodograph*, convergence along the RFGF is enhanced as the cold outflow intercepts strong south-southeasterly low-level flow. Horizontal shear along the density current interface manifests itself as a sheet of positive, cyclonic vorticity and the transition zone's width is minimized due to enhanced convergence. Strong, but small and numerous vortex features develop within the transition zone in this environment. (b) In the case of a low-level wind shear layer characterized by a *clockwise-curved hodograph*, the outflow intercepts the same low-level environment but with relatively weaker convergence. Even though horizontal shear across the density current interface still manifests itself as a sheet of cyclonic vertical vorticity, the width of the transition zone is larger because of the weaker convergence. With the added support of storm-relative helicitiy, a few relatively large vortex features develop within the transition zone in this environment. If downdraft-induced wind shear and helicity tilting is responsible for the low-level kinematic features in the NMS-Id simulation, this relationship should be obvious in the idealized downdraft experiments.

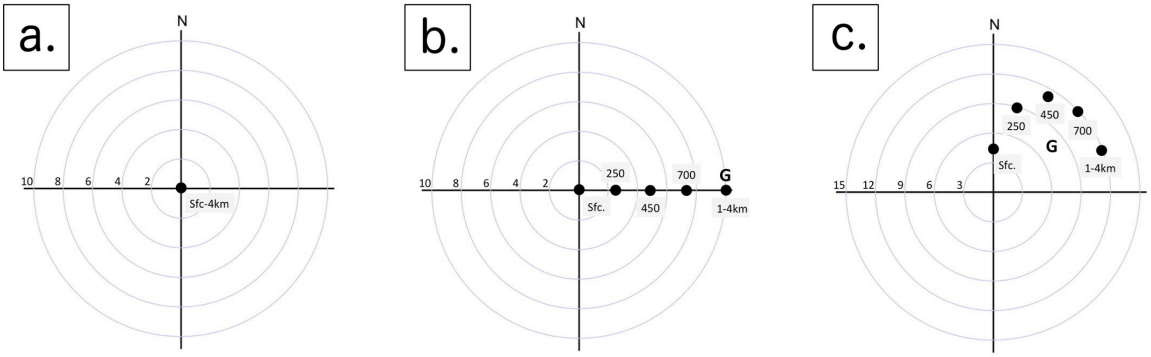

Figure 4.2: Hodographs for each of the horizontally homogeneous vertical wind shear profiles used in the idealized downdraft simulations. (a) A completely static initialization. (b) A linear, unidirectional sheared vertical wind profile where westerly momentum increases from 0–1 km in the domain. The symbol "G" indicates the motion of the model grid. (c) An idealized, directionally sheared vertical wind profile where relatively weak southerly flow increases in magnitude and veers with increasing height to a southwesterly orientation at mid-levels (above 1 km). The symbol "G" is the same as in (b).

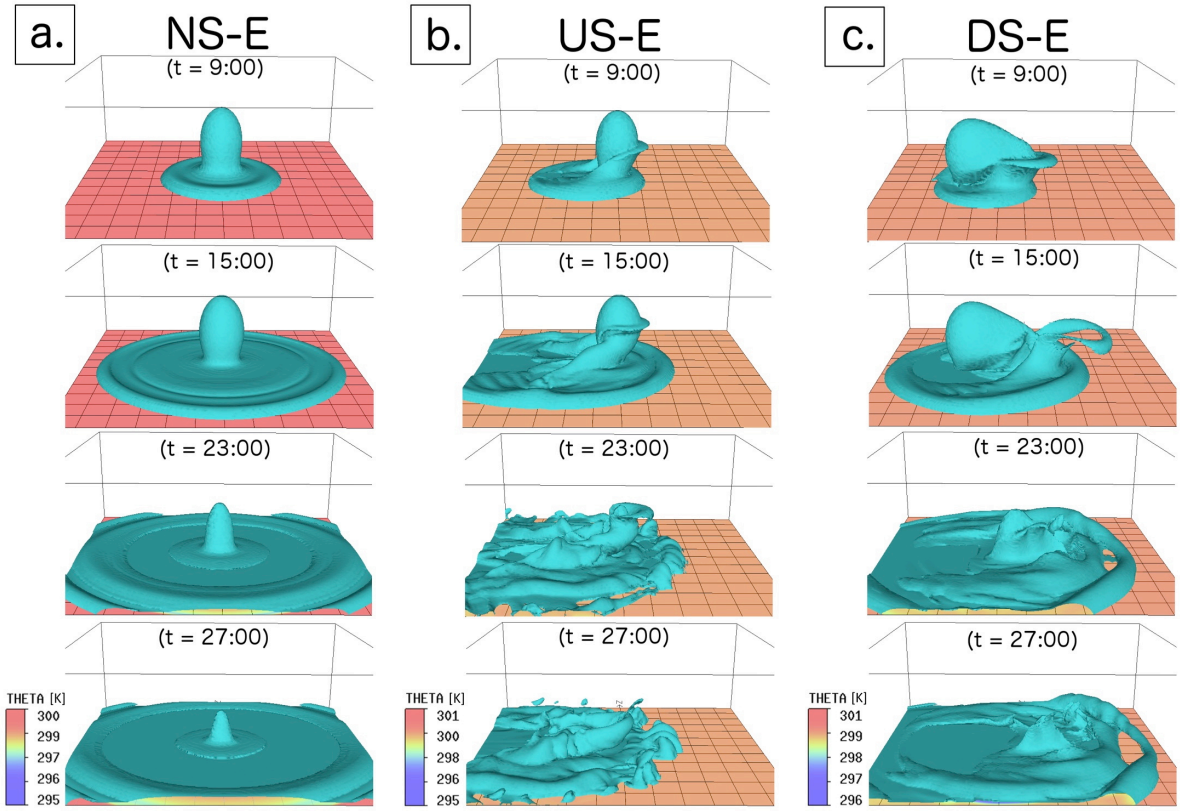

Figure 4.3: Three-dimensional isosurfaces of -0.1 K potential temperature in the (a) NS-E, (b) US-E and (c) DS-E simulations at times 9 min (*top row*), 15 min (*second row*), 23 min (*third row*) and 27 min (*bottom row*) from model initiation as viewed from the South. In all of the images, surface potential temperature is plotted as a colored horizontal cross section whose temperature scale can be seen at the bottom of each column of images. Black boxes with an area of roughly 1 km^2 are plotted against the surface potential temperature horizontal cross section to provide a sense of spatial scale.

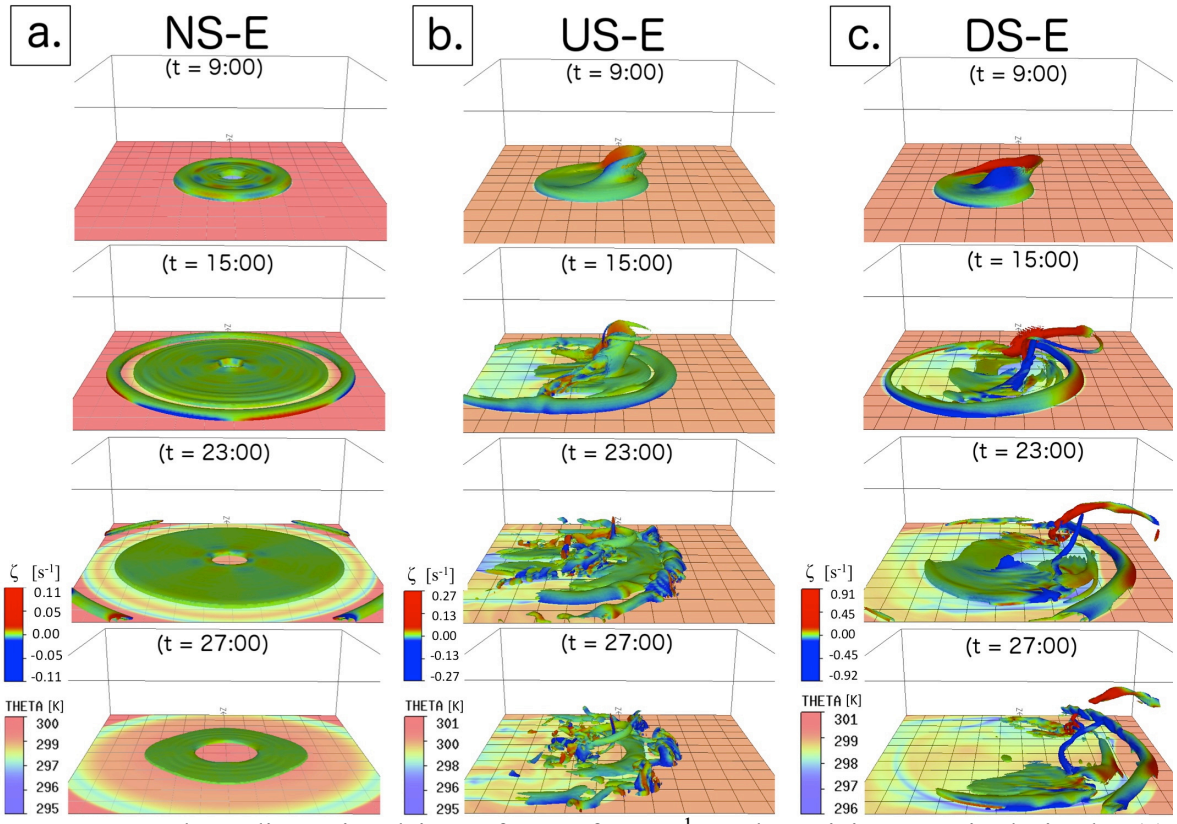

Figure 4.4: Three-dimensional isosurfaces of .04 s^{-1} total vorticity magnitude in the (a) NS-B, (b) US-B and (c) DS-B simulations at times 9 min (*top row*), 15 min (*second row*), 23 min (*third row*) and 27 min (*bottom row*) from model initiation as viewed from the South. These isosurfaces are colored as in Figure 3.1b. In all of the images, surface potential temperature is plotted as a colored horizontal cross section whose temperature scale can be seen at the bottom of each column of images. Black boxes with an area of roughly 1 km^2 are plotted against the surface potential temperature horizontal cross section to provide a sense of spatial scale.

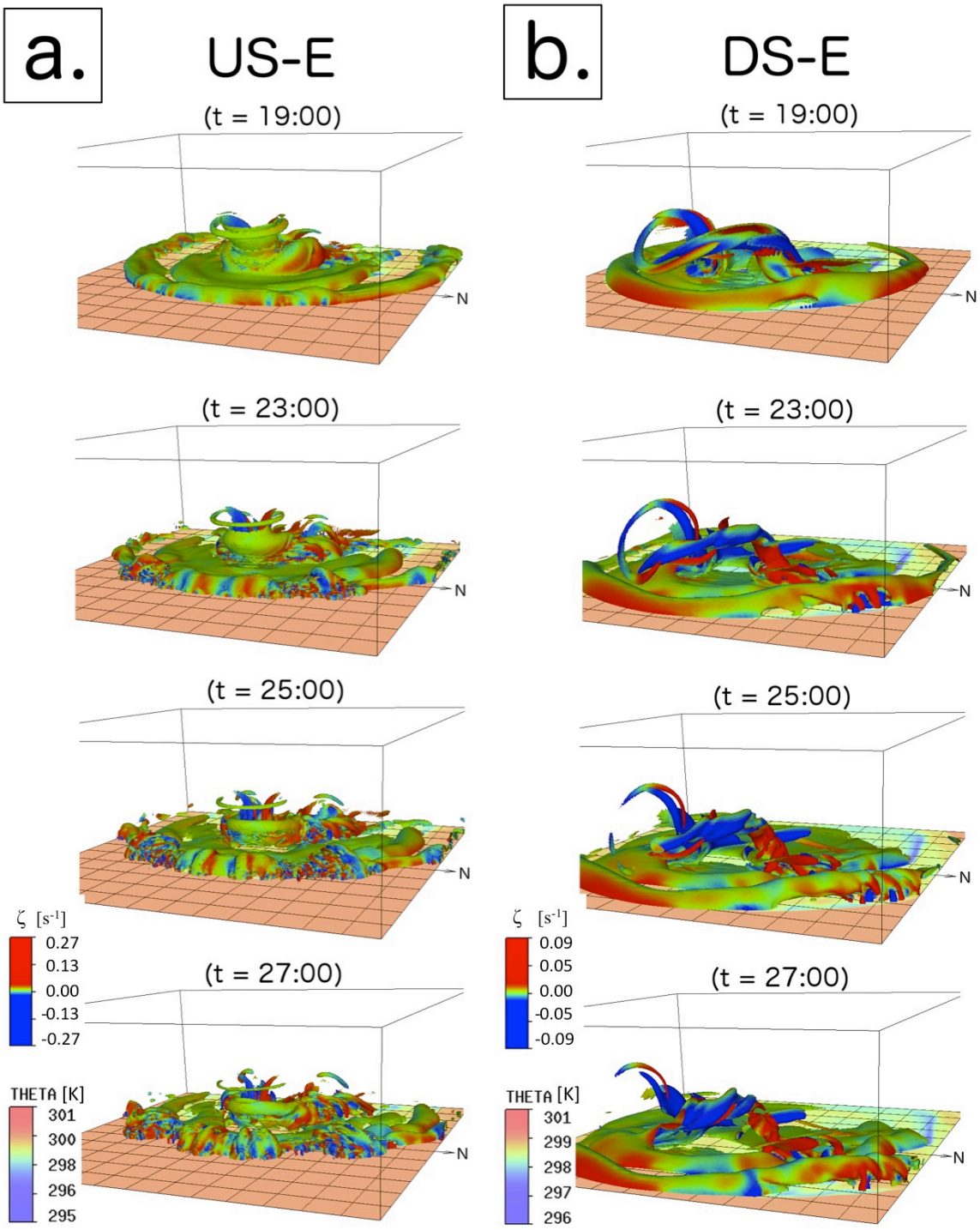

Figure 4.5: Same as Figure 4.4 except the three-dimensional isosurface value of total vorticity has been increased to .02 s^{-1} and the simulated domain is viewed from a Notheastern vantage point. Also observe the change in simulation time for each image in (a) and (b).

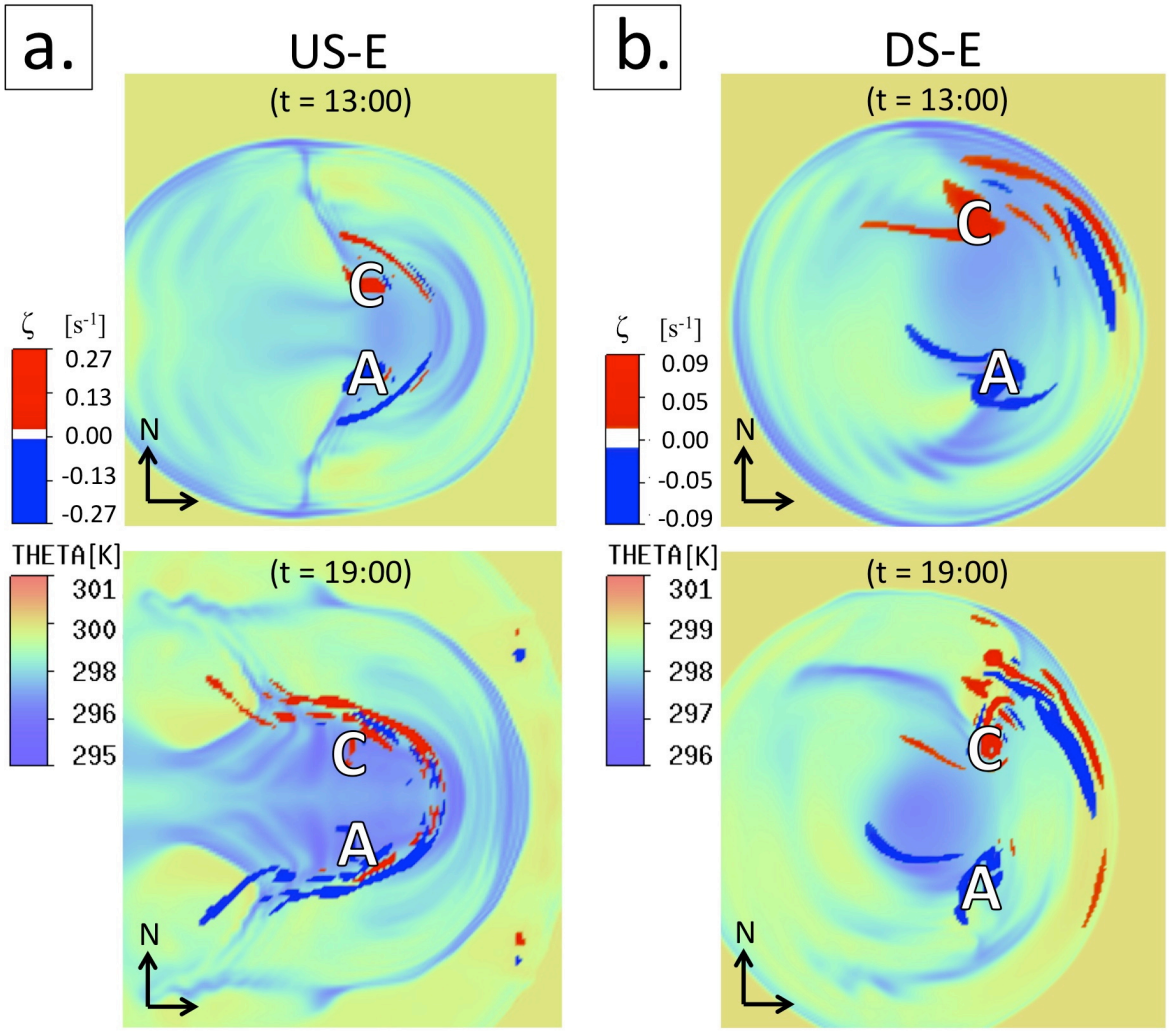

Figure 4.6: A top view of the (a) US-E and (b) DS-E simulated domains 13 min (*top row*) and 19 min (*bottom row*) after model initiation. The background in each image is colored by surface potential temperature and the foreground color in each image corresponds to near-surface (less than 300 m AGL) vertical vorticity values of > 0.1 s^{-1} (red) and vertical vorticity values < -0.1 s^{-1} (blue). The "C" and "A" labels in each image stand for "cyclonic" and "anticyclonic", respectively.

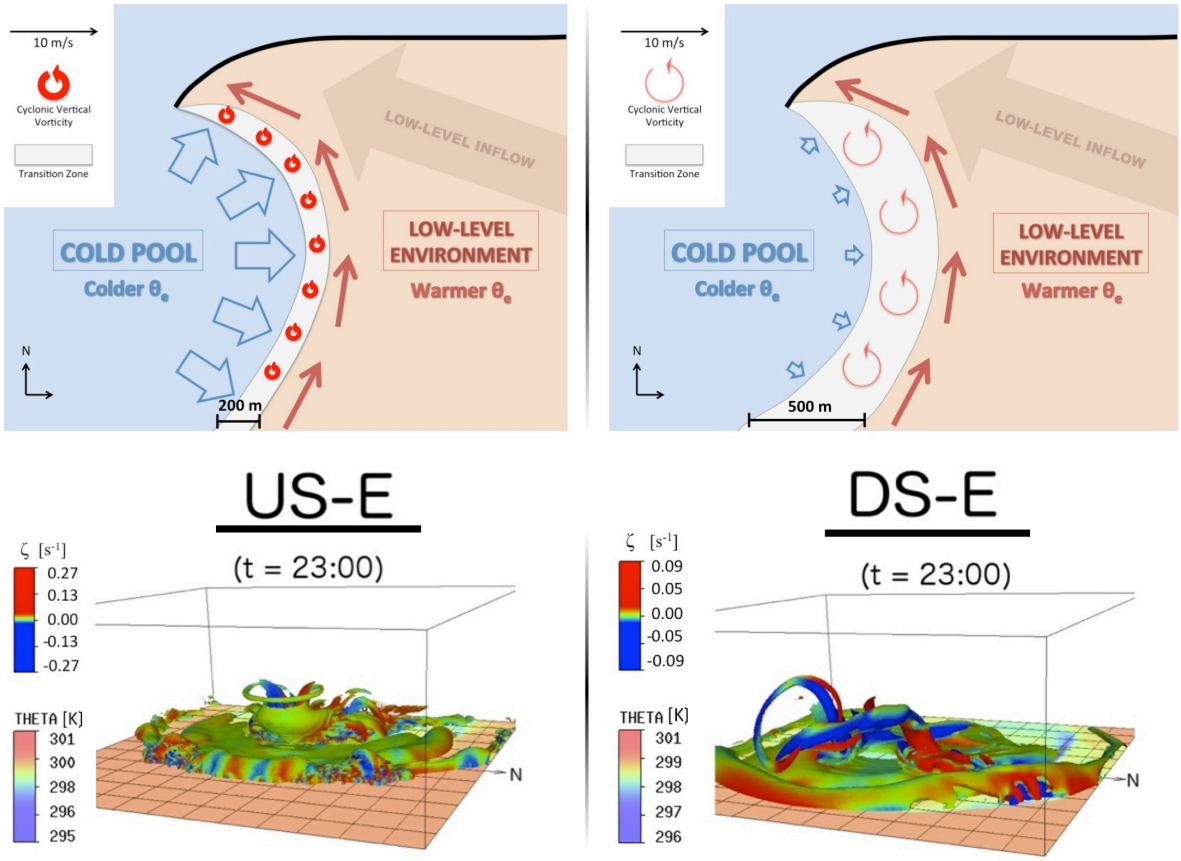

Figure 4.7: A comparison between the predicted and final results of the idealized downdraft simulations. (*Top Row*) The predicted results as they were presented in Figure 4.1. (*Bottom Row*) The downdraft experiment results after 23 min of simulation time as they were presented in Figure 4.5. (*Left Column*) Environments with a unidirectionally sheared, or straight-line hodograph, low-level wind profile. (*Right Column*) Environments with a directionally sheared, or clockwise-curved hodograph, low-level wind profile.

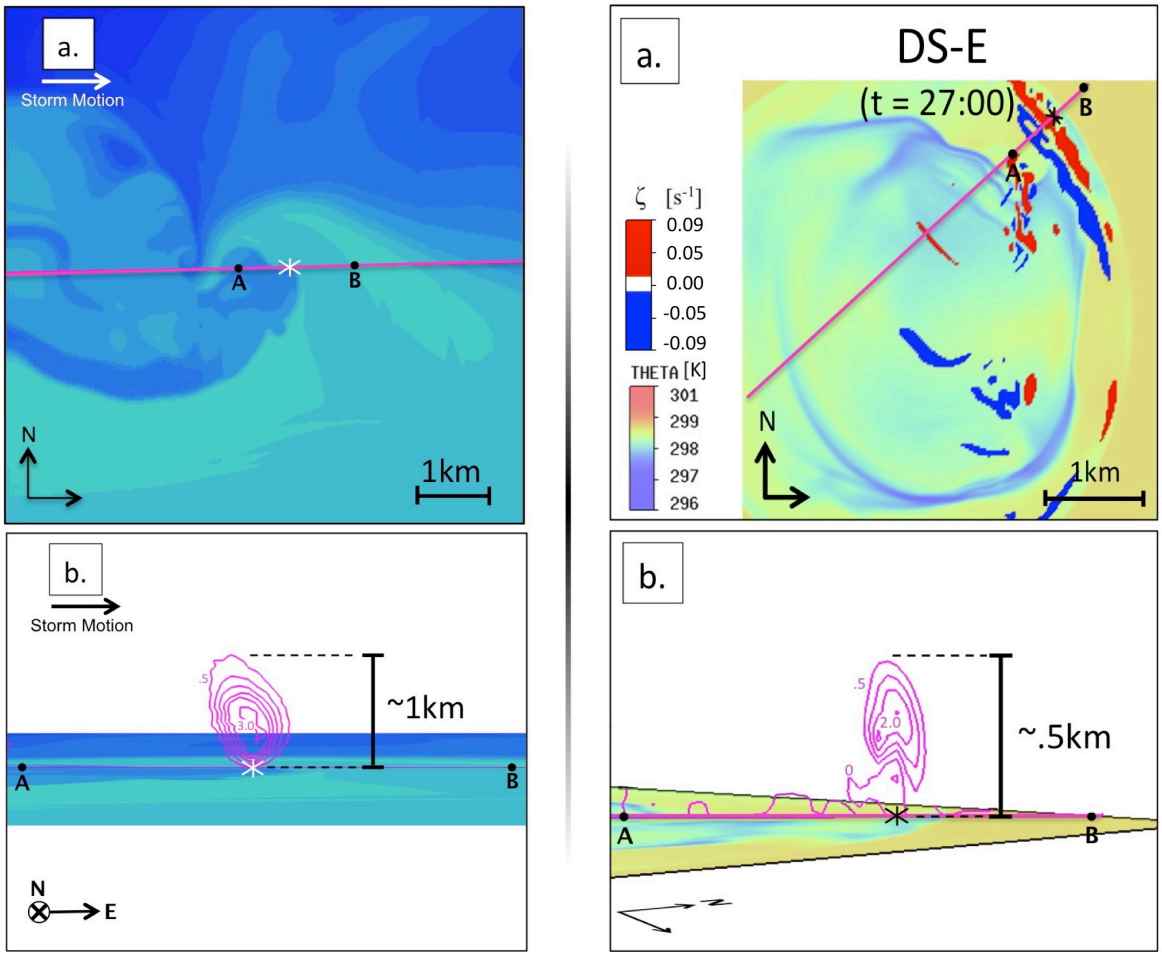

Figure 4.8: A comparison between the vertical stretching of vortex sheet roll-ups in the the NMS-Id simulation and the DS-E idealized downdraft simulation. (*Left Column*) The NMS-Id results are presented as they were in Figure 3.3. (*Right Column*) The DS-E idealized downdraft results as they were presented in Figure 4.6 with a vertical cross section (magenta line) of the same stretching quantity shown in Figure 3.3. Note the vertical height of the roll up in the DS-E simulation is half that of the roll-up in the NMS-Id simulation.

Chapter 5: Sensitivity Experiments

This chapter discusses the results of a series of experiments performed to test the sensitivity of the idealized downdraft simulation results in Chapter 4 to the model's configurations. Three aspects of the simulations were modified. The first was the thermal perturbation definition (cooling function parameterization); the second was the depth of the low-level wind shear layer, and the third was the affect of surface friction. Each sensitivity experiment is discussed individually in separate sections that begin with a brief discussion of how the model was configured to perform that section's sensitivity test.

a. Thermal Perturbation Definition

There were two key aspects of the thermal perturbation used in the idealized downdraft experiments of Chapter 4. First, it was a cooling function that, over a specified time interval, continually generated negatively buoyant air to force a sustained downdraft. Second, it had the geometric shape of a prolate ellipsoid. In this sensitivity experiment, tests were performed to investigate the relative importance of each of these thermal perturbation characteristics to the idealized downdraft simulation results.

Two different cooling function definitions were used for this analysis. Both were defined using the same thermal perturbation definition of (1) and (2) in Chapter 3a, but changed one of the two key aspects of the thermal perturbation used in Chapter 4. The first (hereafter referred to as the *bubble perturbation*) was defined to remove the effect of the cooling function. It therefore instantiated the same prolate ellipsoid at time $t = 0$ s as a potential temperature perturbation of -3 K from which time the cooling function was turned off to allow the initial bubble to evolve without any additional forcing. The second

thermal perturbation (hereafter referred to as the *disk cooling function*) was defined to have an inflated horizontal radius and compressed vertical radius to produce a thermal perturbation with an initial, oblate-ellipsoid-shaped cooling "layer". This was achieved by setting $h_x = h_y = 3000$ m and $h_z = 200$ m in (1) from Chapter 3a.

The same three vertical wind shear profiles displayed in Figure 4.2 were used as a horizontally homogeneous kinematic field initialization and both thermal perturbations were positioned directly above the 1 km deep shear layer in the same way the ellipsoid thermal perturbations were in Chapter 4. For simplicity, each of the simulations was given a name that represented the wind shear profile and thermal perturbation used in the simulation. The naming convention used was the same as in Chapter 4. Since the same wind shear profiles were used in this sensitivity analysis, the simulation names ending in "B" correspond to those using the bubble perturbation and the simulation names ending in "D" correspond to those using the disk cooling function. The results of these experiments are discussed below and, in the interest of concision, only the vorticity evolution will be presented for each experiment.

Figure 5.1 shows the results of the bubble perturbation experiments using the three low-level vertical wind shear profiles in Figure 4.2. To first order, the results appear very similar to those of the idealized downdraft experiments shown in Figure 4.4. When vertical wind shear was added (Fig. 5.1b and Fig. 5.1c), an elongated, towering arched vortex tube manifested itself in the domain and vertical vorticity magnitudes in the domain were increased. However, in addition to being much less noisy, there are two distinctions worth mentioning.

First, the only obvious, prominent outflow boundary vortex sheet with positive, vertical vorticity along its leading edge was in the DS-B simulation (Fig. 5.1c) when a clockwise-curved hodograph was used. By the oppositely signed vertical vorticity values on both sides of the vortex sheet, this sheet appeared arched over the outflow boundary. There was some signature of a vortex sheet in the US-B simulation that employed a straight-line hodograph, low-level wind shear layer, but it did not show any indication of possessing positive, vertical vorticity. It was also quickly outran by the towering arched vortex tube that was moving with the mid-level westerly winds aloft which did not appear to be the case in the US-E simulation (Fig. 4.4b). This latter point can be reasoned given that there was not as strong of a pressure acceleration from the base of the subsiding cold pool compared to when a sustained downdraft was forced aloft. The surface outflow's propagation speed was then only a function of its original momentum, which upon reaching the surface, was weakened due to convergence with the low-level momentum of the environment.

Second, the outflow boundary vortex sheet in the DS-B simulation was shallow compared to the DS-E simulation. In the DS-B simulation (Fig. 5.1c) the summit of the vortex sheet reached only around 250 m, which is roughly half the height of the vortex sheet's summit in the DS-E simulation (Fig. 4.4c). Since the depth of the outflow leading head's circulation is related to the propagation speed of the outflow relative to its environment, and the outflow's propagation speed is a function of the cold pool's baroclinicity magnitude (Markowski and Richardson 2010), the colder the downdraft is, the deeper the leading head circulation will be. A deeper leading head circulation

consequently raises the height of the arched vortex sheet's summit if the vertical wind shear profile remains unchanged. Compared to the -3 K potential temperature perturbation used in this chapter's bubble experiments, the ellipsoid cooling function thermal perturbations used in Chapter 4 generated slightly colder air (~ 1 K cooler) over the course of the 16 minutes that the cooling function was turned on and the same environmental wind shear profile was used (compare the scale bar in Fig. 4.4 to Fig. 5.1). Therefore, given the relationship between the outflow leading head's circulation and baroclinicity magnitude, it is expected that the DS-E simulation's arched vortex sheet possessed a higher summit height.

Outflow boundary vortex sheets were observed in the disk cooling function simulation as well (Fig. 5.2). The experiments using this thermal perturbation type employed the same cooling function as the idealized downdraft experiments in Chapter 4 with the only exception that the cooling function took the geometric shape of an oblate ellipsoid and not a prolate ellipsoid. Therefore, if the height of the arched vortex sheet's summit in the DS-B and DS-E simulations was a consequence of the depth of the outflow leading head's circulation, which in turn depends on the baroclinicity magnitude of the outflow, the height of the arched vortex sheet's summit in the DS-D simulation (Fig. 5.2c) should have been the same as the DS-E simulation. Closer inspection revealed that the vortex sheet along the outflow in the DS-D simulation was, indeed, around the same height of 500m. While this discussion is enlightening in the distinction it makes between the DS-E and DS-B idealized downdraft simulations, it ultimately provides further evidence that

the vortex sheet seen in the NMS-Id simulation (Fig. 3.1) of Chapter 3 was arched because of the outflow density current leading head's circulation.

b. Wind Shear Layer Depth

To isolate the influence of the shear layer's depth in each simulated environment prescribed with a directionally sheared vertical wind profile (clockwise-curved hodograph; see Fig. 4.2c), the height of the shear layer was raised to roughly 2 km (Fig. 5.3) and the thermal perturbation center was also raised to remain initialized above it. The thermal perturbation used was the same prolate ellipsoid from the idealized downdraft experiments of Chapter 4. In this simulated environment, the model grid was defined to move with the mid-level (~ 1 km) southwesterly flow and representation of this grid motion can be seen in Figure 5.3a as the symbol, "G". Only the simulations using a directionally sheared vertical wind profile and elliptical cooling function were tested since this experiment most closely replicated the low-level pre-tornadogenesis environment of the NMS-Id simulation.

Figure 5.4 shows that, when shear layer depth was increased, the low-level environment possessed much higher magnitudes of cyclonic and anticyclonic vertically oriented vorticity. It is intriguing to note, though, that this strong vorticity did not immediately appear to be situated along the cold outflow boundary when viewed from the south (Fig. 5.4). A vertically elongated arched vortex tube, seen in both the original shallow (Fig. 5.4a) and deep (Fig. 5.4b) shear layer simulations, appeared to possess the highest vorticity magnitudes. However, viewing from the northeast (Fig. 5.5) revealed that the maximum positive vertical vorticity in the domain was actually situated on the

periphery of the surface outflow at its northeastern edge in the form of discrete arched vortex tubes (Fig. 5.5b).

In addition, the region along the surface outflow boundary where the most appreciable horizontal shear (vertical vorticity) resided, shifted counterclockwise to the northern and northeastern edges of the outflow boundary. It was here that the arched vortex tubes were situated as a result of shear instabilities leading to the same vortex sheet roll-up processes observed in the original, shallow shear layer DS-E simulation. Thus, the primary result of the simulations using a shallow and deep wind shear layer showed that vertical vorticity magnitudes were increased due to vortex sheet roll-ups along the northeastern edge of the simulated outflow boundary in the experiment using a deeper wind shear layer.

A final comparison of the shallow shear layer and deep shear layer experiments in Figure 5.5 reveals that the vortex sheet roll ups along the outflow boundary in the deep shear layer experiment were far more numerous than in the shallow shear layer experiment. In a general sense, the northeastern edge of the outflow boundary in the deep shear layer experiment appeared somewhat similar to the US-E (unidirectional shear–ellipsoid) idealized downdraft experiment (Fig. 4.5a). Recall that, in the US-E experiment, there was no low-level, Storm Relative Helicity (SRH) to support the upscale growth of developing vortex tubes along the US-E's simulated outflow boundary. The resulting vortex features in the US-E simulation remained isolated from one another and were far more numerous compared to when an environment with low-level SRH was used.

However, in the deep shear layer experiment, there is appreciable SRH given the directionality of the wind shear over the layer's depth. The most important distinction to make between the shallow and deep shear layer experiments, though, is the difference in magnitude of 0-1 km SRH. This is because the heights of the vortex features along the outflow boundary need to be comparable to the depth of the shear layer for helicity tilting by the downdraft to have its maximum vertical stretching effect. Since, in both shear layer depth experiments the height of the vortex sheet roll-ups were roughly 500 m, it is the 0-1 km SRH of the simulated environment that is most important to the developing vortex features along the outflow boundary. Comparing the 0-1 km SRH characteristic of both the shallow and deep shear layer experiments in Figure 5.3b and Figure 5.3c reveals that the deep shear layer experiment possessed half the 0-1 km SRH of the shallow shear layer experiment. Therefore, vortex tubes along the outflow boundary in the deep layer case could not grow upscale via low-level vertical vorticity aggregation as much as in the shallow shear layer case. This exposes an important relationship between the height of the arched vortex sheet's summit and the low-level SRH in the idealized downdraft experiments while also inferring the sensitivity of the roll-up process in the idealized tornadogenesis simulation (Fig. 3.2) to the low-level environmental SRH.

c. Surface Friction

Since every simulation performed thus far employed a free-slip lower boundary condition, experiments were conducted to isolate the influence of surface friction on the observed vortex sheet and vortex sheet evolution in the DS-E idealized downdraft simulation (Fig. 4.2c). Surface friction was incorporated into this experiment using the

same surface-layer parameterization used in the idealized tornadogenesis simulation of Chapter 3 defined by Louis (1979). The results of this experiment can be seen in Figure 5.6.

Via the provided scales in Figure 5.6 it is obvious that, when the surface friction parameterization was turned on, the magnitudes of vertical vorticity remained relatively unchanged and a similar outflow boundary vortex sheet was visible after around 20 min of simulation time. However, the structure of the vortex sheet was slightly modified. Specifically, the summit of the vertically arched vortex sheet 23 min into the DS-E simulation without surface friction (Fig. 5.6a) was roughly 250m lower than when surface friction was turned on (Fig. 5.6b).

This result can, again, be explained by invoking density current dynamics. The shallower modes of the density current, which propagate proportionately to a gravity wave phase speed with the same equivalent depth, are slowed via surface drag. A density current's interaction with the ground therefore leads to a forward tilt of its leading edge interface (outflow boundary) with the surrounding environment (Markowski and Richardson 2010). Static instability arises on the leading edge of the density current as a result of this forward tilt and overturning re-organizes the outflow boundary into a more vertically erect orientation than would be the case if surface friction were neglected. Therefore, the vortex sheet in Fig 5.6b arched considerably more in the vertical as a result of the increased depth of the outflow density current's vertically erect leading head. This insight is an important aspect of this sensitivity experiment's results as it demonstrates the

role of surface drag in forming more vertically erect arched vortex sheets along the outflow boundary of the idealized tornadogenesis simulation in Chapter 3.

d. Summary

The results presented in this chapter further illustrated that a downdraft's reorientation of environmental wind shear via vertical tilting can, to first order, produce the low-level kinematic environment seen in the NMS-Id simulation. In addition, key relationships between the idealized downdraft experiment's model configuration and results were exposed as a result of these experiments. These relationships yielded important insights about how the idealized tornadogenesis simulation's (NMS-Id's) environmental characteristics influenced the low-level pre-tornadogenesis dynamics presented in Chapter 3.

When the thermal perturbation definition was modified, results showed that increasing the baroclinicity magnitude of the thermal perturbation resulted in outflow boundary vortex sheets that arched higher in the vertical direction. Since the depth of the outflow density current's leading head circulation increases with increasing outflow baroclinicity (Markowski and Richardson 2010), it was reasoned that the vortex sheets appear arched because of an underlying leading head circulation that can increase, or decrease, in vertical depth depending on the baroclinicity of the surface outflow. This provided further evidence that the Rear Flanking Gust Front (RFGF) vortex sheet in the NMS-Id simulation (Fig. 3.1b) was arched because of an underlying leading head circulation associated with the cold, surface outflow from the storm's Rear Flanking Downdraft (RFD).

Increasing the depth of the prescribed wind shear layer resulted in a low-level kinematic environment that resembled the unidirectionally sheared, ellipsoid thermal perturbation (US-E) idealized downdraft experiment (Fig. 4.5a). This was rationalized as a consequence of the decreased 0-1 km SRH when the shear layer depth was increased. Since the vortex sheet's summit reached a height of around 500 m, its upscale growth benefited from the 0-1 km SRH and not the 0-2 km SRH tilted by the downdraft and focused along the outflow boundary. Consequently, when the shear layer depth was increased, vortex sheet roll-ups did not have appreciable support from the decreased 0-1 km SRH to aggregate surrounding vorticity. Numerous vortex features were then manifested along the outflow boundary. This provided an important insight into role of low-level SRH in the pre-tornadogenesis dynamics of the NMS-Id simulation.

Finally, when surface friction was turned on, the outflow boundary vortex sheet appeared to arch considerably more in the vertical direction. Density current dynamics were again used to justify this result. As the outflow density current interacts with the ground, surface drag results in a more vertically erect leading head. Since the vortex sheet appeared to stretch more vertically when surface friction was added, it was concluded that it was because of the underlying leading head circulation that the sheet was subsequently arched over. The relationship between surface friction and vortex sheet summit height in this sensitivity experiment further justified the assertion that outflow boundary vortex sheets appear arched because of the outflow density current leading head's circulation.

The results of this chapter ultimately helped explain the role of downdraft-induced wind shear and helicity tilting in the pre-tornadogenesis dynamics of the NMS-Id

simulation. On the other hand, a major distinction between all of the idealized downdraft experiments and the NMS-Id simulation is that tornadogenesis was only observed in the supercell environment of the NMS-Id simulation. The following chapter concludes this thesis with a discussion on the likely role of a mesocyclone in organizing the vortex sheet roll-up process and supporting the upscale growth of low-level vertically oriented vorticity to tornadic strength.

Chapter 5 Figures

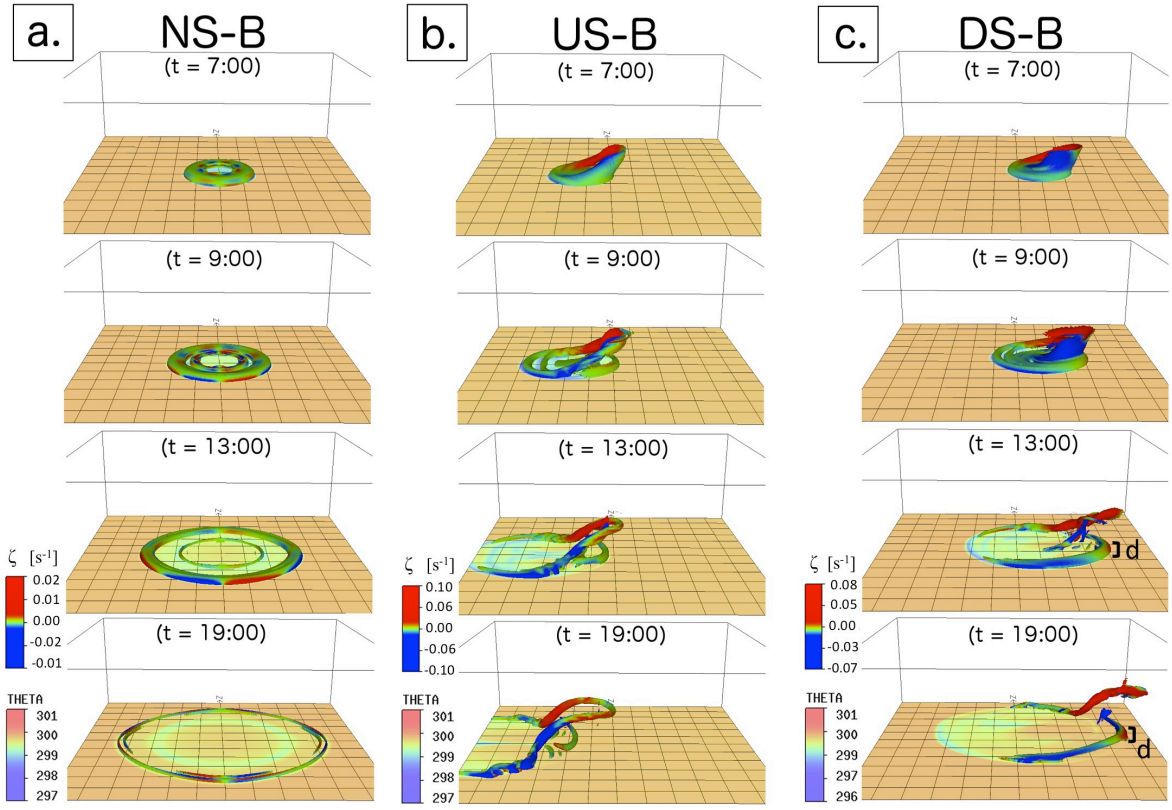

Figure 5.1: Same as in Figure 4.4, but for each of the experiments performed using the bubble perturbation with the three different 0-1 km vertical wind shear profiles in Figure 4.2. (a) No wind shear. (b) Straight-line hodograph. (c) Clockwise-curved hodograph. The symbol "d" in (c) is used to show the depth of the vortex sheet which is approximately 250 m. Notice these figures appear much more clean than in Figure 4.3, owing to the fact that cold air is not consistently being generated aloft in this sensitivity experiment.

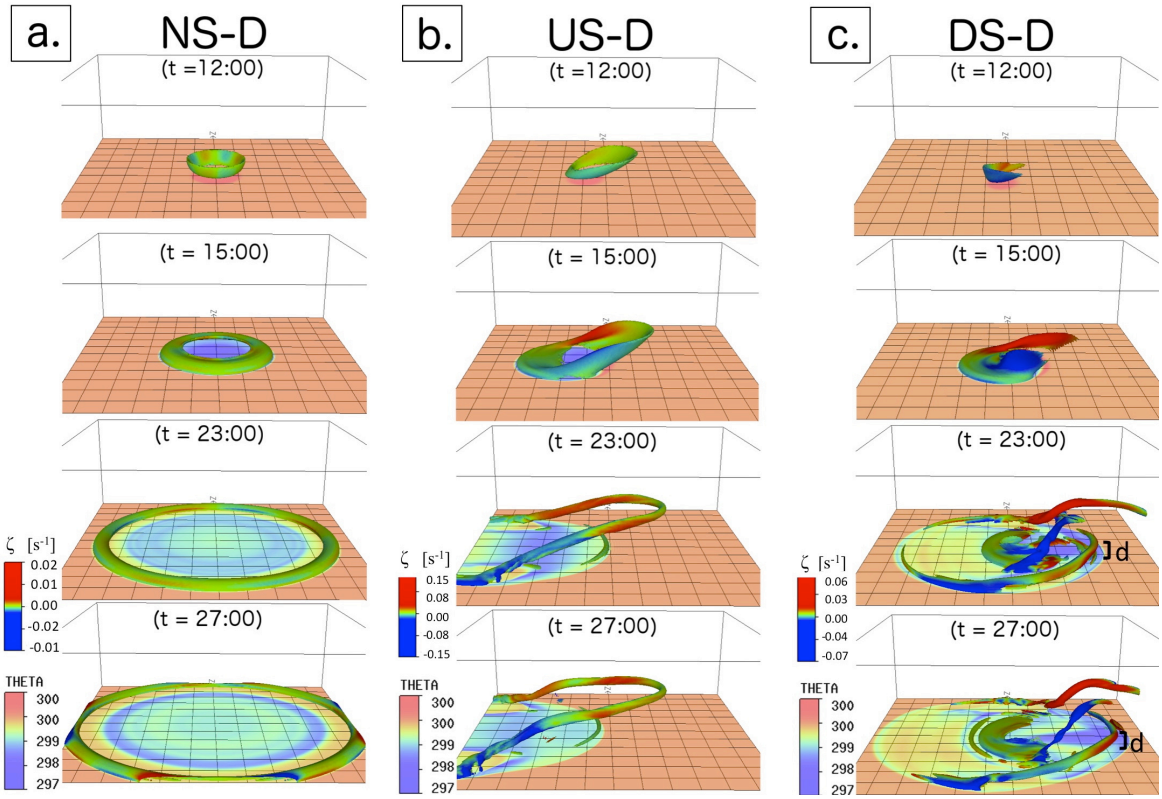

Figure 5.2: Same as in Figure 5.1 but using the disk cooling function thermal perturbation. The symbol "d" in (c) is used to show the depth of the outflow boundary vortex sheet, which is approximately 500 m. This is roughly equivalent to that of the DS-E simulation (Fig. 4.4c) and twice that of the DS-B simulation (Fig. 5.1c).

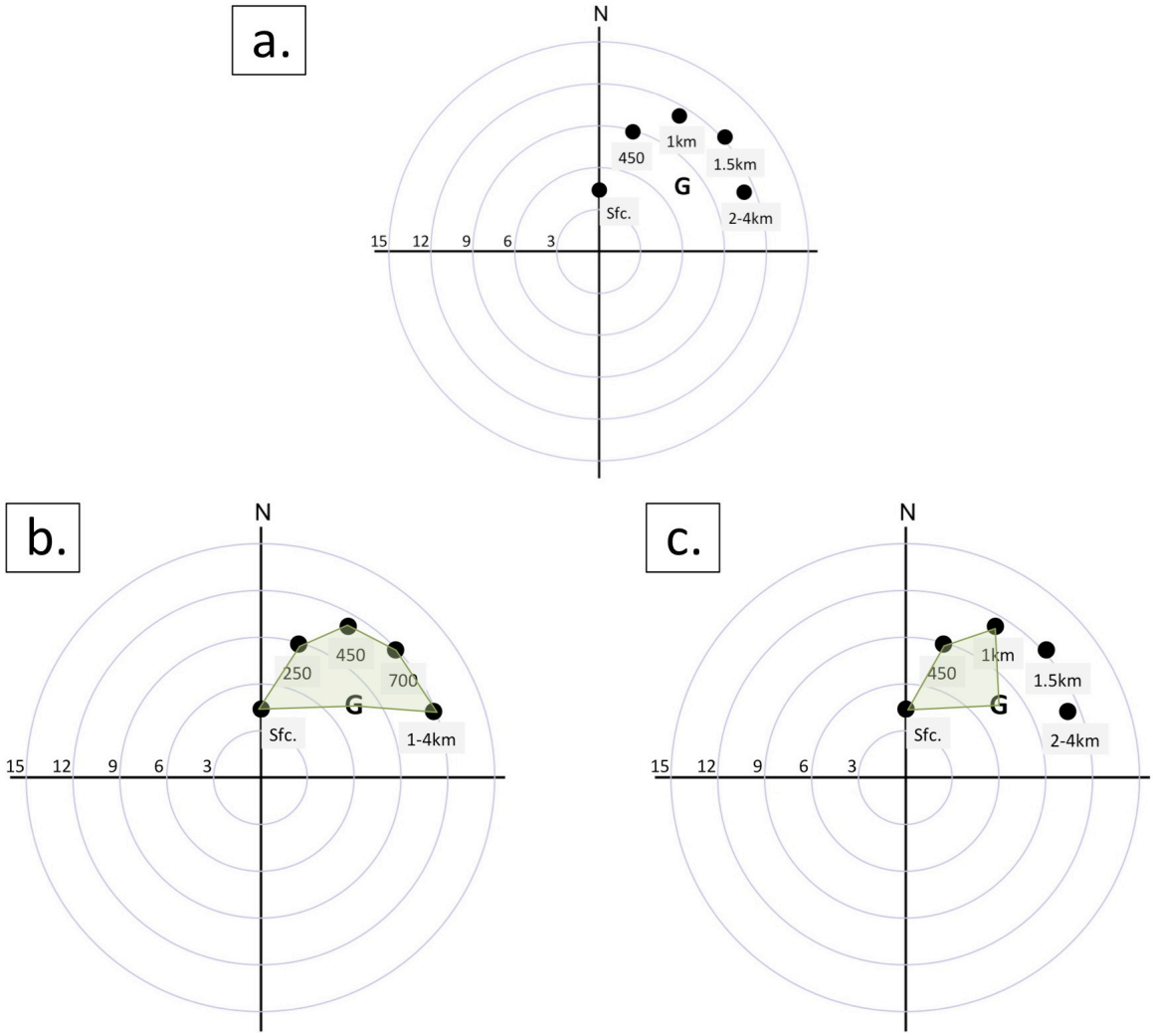

Figure 5.3: (a) Hodograph representing the vertical wind shear layer prescribed for the sensitivity experiment where the depth of the shear layer is increased from 1 km to 2 km. (b) Hodograph from the original DS-E simulation using a 0-1 km wind shear layer. The green fill shows the 0-1 km Storm Relative Helicity (SRH) characteristic of this wind shear layer. (c) Same hodograph as in (a) with its 0-1 km SRH shown in green fill. Notice the shape and orientation of the hodograph remains unchanged between (b) and (c) and it is only the depth of the layer that is modified. This effectively decreases the 0-1 km SRH in the deep shear layer case (compare (b) to (c)).

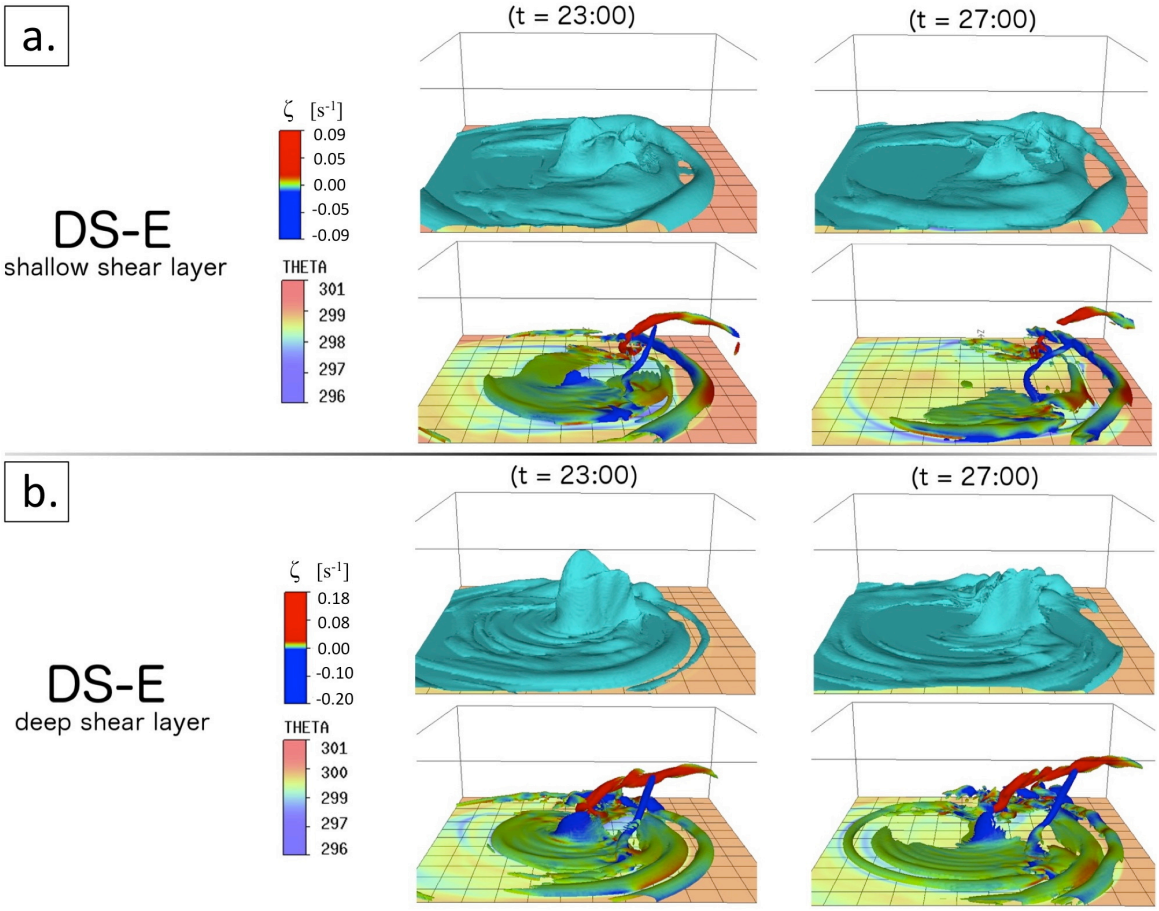

Figure 5.4: (a) DS-E simulation results showing (*top-row*) the thermal perturbation evolution after 23 min and 27 min of simulation time, and (*bottom row*) the vorticity evolution displayed as in Figure 5.2 after 23 min and 27 min of simulation time. (b) Same as (a), but for the simulation using a deeper shear layer (Fig. 5.3a). Notice there appears to be more vertically oriented vorticity situated along the eastward edge of the outflow boundary in (a) as opposed to (b).

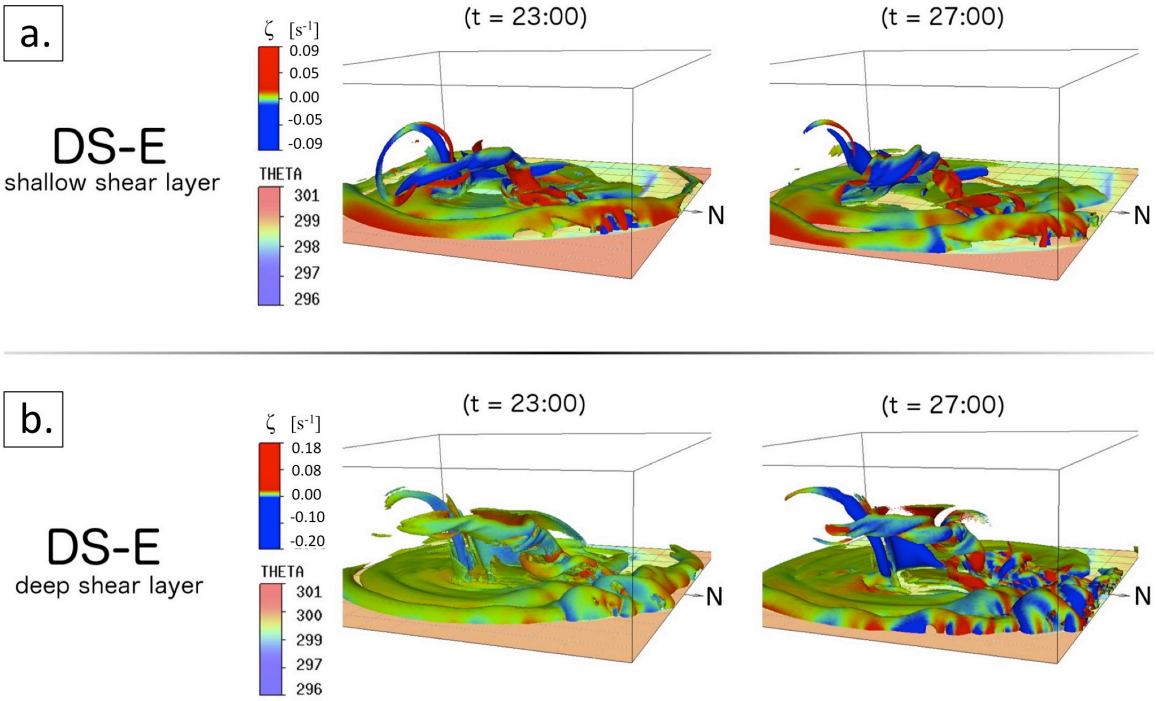

Figure 5.5: (a) Northeastern view of the DS-E simulation's vorticity evolution, as shown in Figure 4.5, 23 min and 27 min into the simulation. (b) Same as (a) but for the simulation using a deeper wind shear layer (Fig. 5.3a). Notice the vorticity distribution along the northeastern edge of the outflow boundary in (b) after 27 min of simulation time appears quite similar to the US-E simulation in Figure 4.5a.

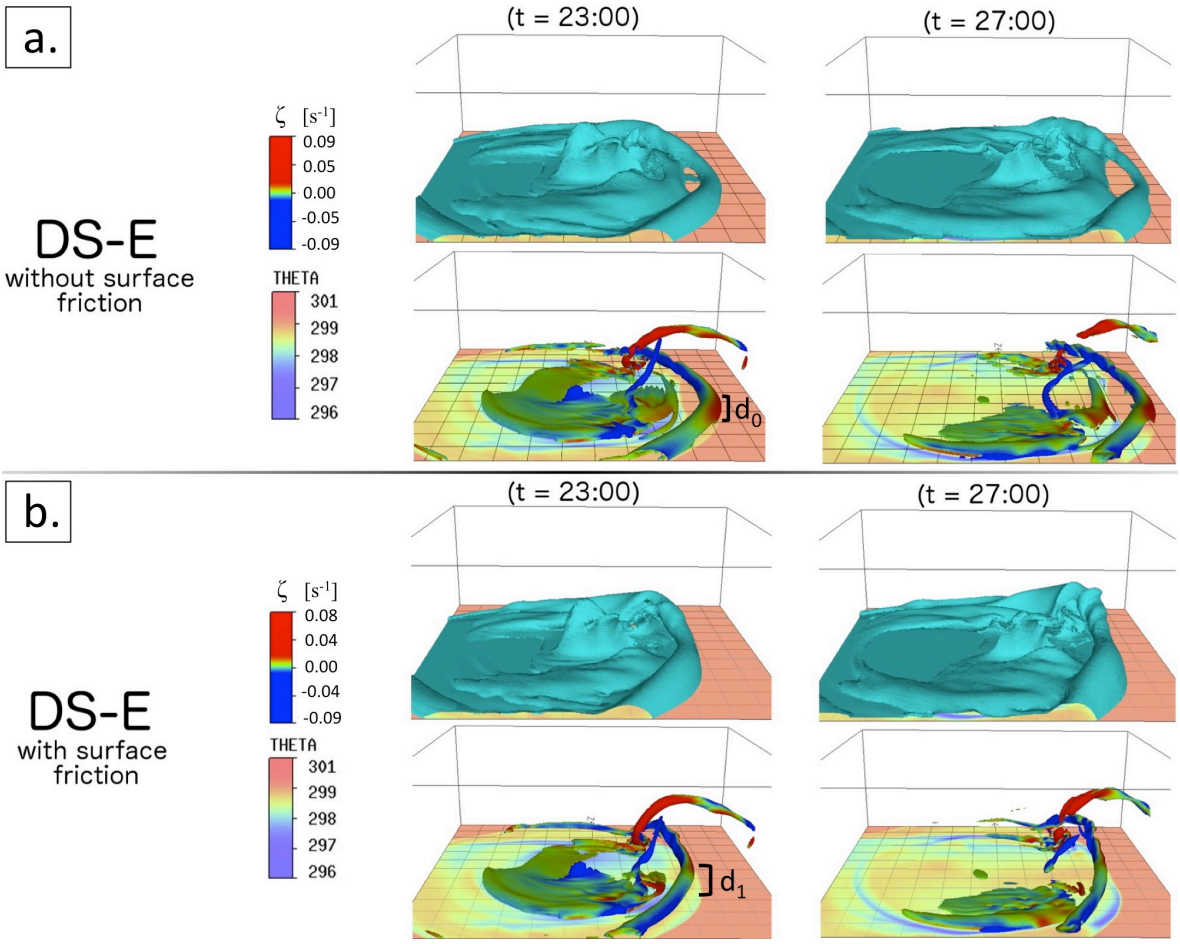

Figure 5.6: (a) DS-E simulation results as shown in Figure 5.4a. (b) DS-E simulation results displayed as in (a) after 23 min and 27 min of simulation time when a surface friction parameterization defined by Louis (1979) was turned on. The symbols "d_0" in (a) and "d_1" in (b) are used to show the depth of their corresponding vortex sheets. After investigating these values it was found that, d_0 was roughly 500 m and d_1 was roughly 250m.

Chapter 6: Concluding Summary and Discussion

It was the hypothesis of this thesis that downdraft tilting of environmental wind shear was likely an important dynamical process leading to tornadogenesis. The results showcased in this thesis appear to verify that hypothesis. Furthermore, analysis of these results revealed a dynamical relationship between the growth of low-level vertical vorticity and the low-level SRH, which is an unexplained relationship using current vortex line arching models of tornadogenesis (e.g. M08).

It has been shown that a vortex sheet roll-up process along a storm's Rear Flanking Gust Front (RFGF) preceded tornadogenesis in a numerical simulation of a tornado-producing supercell (NMS-Id). Resulting vortex tubes appeared arched over the cold pool associated with the storm's Rear Flanking Downdraft (RFD) in the same way the original vortex sheet was arched. Persistent vertical stretching of an ideally-located arched vortex tube near the rear and forward flanking gust front cusp aided the tube's upscale growth by enhancing its aggregation of surrounding vertically oriented vorticity until connection with the mesocyclone supported its further maintenance.

Supporting simulations of the simple dry dynamics of a subsiding downdraft through a wind shear layer produced the same arched vortex sheet and vortex sheet roll-up process seen to precede tornadogenesis in the NMS-Id simulation. Thus, the downdraft's role in the pre-tornadogenesis dynamics of the NMS-Id simulation was not necessarily limited to updraft tilting and stretching of its baroclinically-generated vorticity by an updraft-downdraft interaction. Moreover, the arched nature of the vortex sheet and vortex tubes throughout the roll-up process suggests that arched vortex lines in real-world

observations of tornadogenesis events do not immediately indicate an updraft-downdraft interaction as current vortex line arching theory suggests (M08). Sensitivity experiments performed on the idealized downdraft simulations verified that the vortex sheets, and vortex tubes as a result of the sheet's roll-up, were arched because of an underlying, cold outflow density current leading head circulation. Additionally, these sensitivity experiments highlighted the importance of the 0-1 km SRH to the roll-up process in the NMS-Id simulation and, ultimately, tornadogenesis instigation. The ensuing exposition continues this thesis' concluding discussion with the implications that these results have on the current understanding of tornadogenesis.

The results of this idealized numerical study suggest that surface tornadogenesis in a supercell environment can initiate when low-level, ambient horizontal vorticity below the supercell thunderstorm points normal to, and away from, the storm's RFGF. RFD pulses to the surface tilt the initially horizontal vorticity vector vertically upward. The surface horizontal deformation field of the ensuing density current then concentrates positive vertical vorticity along the downshear side of the RFGF, and negative vertical vorticity on the density current's upshear side.

Viewed as vortex lines on a conventional right moving supercell, the low-level shear forms a sheet of horizontally oriented environmental vortex lines pointing toward the east and centered a few hundred meters AGL (Fig. 6.1a). The surface-penetrating RFD bends these vortex lines downward to the surface forming upward pointing vortex lines to the east and downward pointing vortex lines to the west of the RFD (Fig. 6.1b), similar to the depressed vortex line hypothesis of Walko (1993). Upon the RFD reaching the

surface, however, vertical vorticity remains positive all along the ensuing density current's leading edge (or RFGF) and is manifested as a vertically oriented vortex sheet. This vorticity is vertically bent back over the cold pool due to the density current leading head's circulation, ultimately giving the vortex sheet an arched appearance (Fig. 6.1c).

Intensification of low-level vertical vorticity results from the barotropic roll-up of the RFGF's positive, vertical vorticity sheet, agreeing with a dated hypothesis of tornadogenesis presented by Bluestein et al. (2003). However, unlike the hypothesis of Bluestein et al. (2003)'s, resulting vortex tubes along the RFGF retain the orientation of the original vortex sheet and also appear arched. These rolled-up vortices never seem to reach tornadic intensity unless they are formed near the rear and forward flanking gust front cusp in a supercell environment. It is then suggested that there must be special circumstances occurring only in that region for these vortices to strengthen past what appears to be a limit. Previous studies suggest that the ratio of the total swirl to the vertical motion at the top of the swirl, or swirl ratio (e.g. Davies-Jones 1973; see Eq. 1.2), articulates these limits. The existence of a swirl ratio limit is consistent with the simulated strong roll-ups being confined to the gust front cusp, which, as illustrated in Figure 6.1c, is connected to the mesocyclone aloft and is directly below the supercell updraft.

The conceptual model envisioned by the results of this thesis is then the following. As an RFD pulses to the surface, the roll-up process is either initiated, or an existing roll-up process is hijacked whereby surrounding surface vertical vorticity, concentrated in a vortex sheet, is rapidly coiled up to produce a strong surface vorticity center. In this way, the roll-up and aggregation process is actually a mechanism by which the mesocyclone's

vorticity focuses itself to smaller spatial scales near the surface. A graphical illustration of this proposed process is provided in Figure 6.2 to show how it can still explain the existence arched vortex lines and couplets of vorticity in the low-level, pre-tornadogenesis environment of supercell storms. This model solves the dilemma of where the surface vorticity comes from, provides a mechanism for gathering vertical vorticity efficiently and rapidly upon contact with the surface, while also taking into account the likely importance of top-down processes in a supercell environment.

However, further investigation is needed with respect to the dynamical processes leading to mid-level and surface vorticity coupling. The dynamical process(es) leading to the connection of the mesocyclone and misovortices along the RFGF has(have) only been hypothesized here based on this thesis' results. It is then necessary that a study be designed to focus on this connection in order to produce a full conceptual model of a downdraft's role in tornadogenesis. Such an investigation may prove that an updraft-downdraft interaction is an important surrogate for mid-level and surface vorticity connection. Alternatively, analyzing three-dimensional vortex interactions during an RFD pulse may prove to be a more fruitful approach. While the dynamics exposed by such an analysis may yield exciting results, they are left for future investigation.

The roll-up process is ubiquitous in atmospheric dynamics, occurring in hurricane genesis from the ITCZ (Guinn and Schubert 1993; Ferreira and Schubert 1997), non-supercell tornadogenesis (Bluestein 1980; Bluestein 1985; Wakimoto and Wilson 1989; Lee and Wilhelmson 1997a,b; Marquis et al. 2007) and in the mid-upper tropospheric levels of a supercell environment (Odell et al. 2014). Recent literature depicts the reality

of this tornadogenesis process in simulated (Noda and Niino 2005; Noda and Niino 2010) and real-world, tornadic storms (Bluestein et al. 2003; Lee et al. 2012). In a pre-tornadogenesis environment below the supercell storm, this process benefits from the low-level (0-1 km) Storm Relative Helicity (SRH) that supports both its upward extension and the continuous projection of storm scale helicity to the surface. This describes an important link between supercell tornadogenesis and low-level wind shear (e.g. Thompson et al. 2003; Craven and Brooks 2004) and SRH (Markowski et al. 2003) that is not present in baroclinic vortex line arching models of tornadogenesis. Considering this, in combination with the results presented in this thesis, it is likely that the mechanisms responsible for the initiation of supercell tornadogenesis may be dynamically more similar to the barotropic processes typically associated with non-supercell tornadogenesis than originally thought.

Chapter 6 Figures

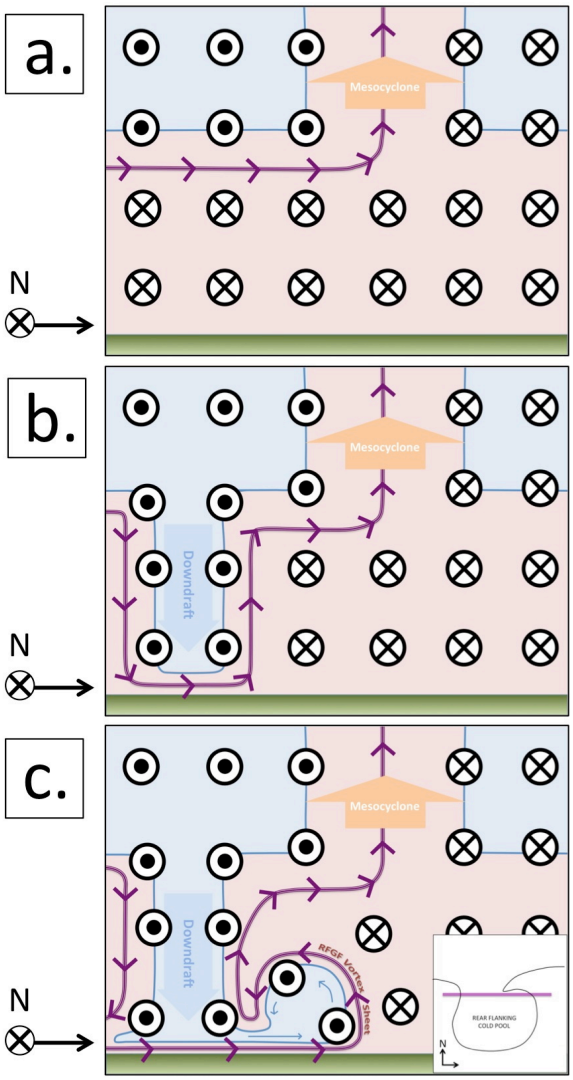

Figure 6.1: Vertical cross sections illustrating the RFGF vortex sheet's genesis where the thick magenta line indicates a single environmental vortex line of the ambient wind shear's vortex sheet. Viewing perspective is from the South. Vectors tails and heads indicate wind velocity into and out of the page, respectively. The small box in the bottom right-hand corner of the figure is a *top-down* view showing the orientation of the cross sections (magenta line) relative to a rear flanking cold pool in (c). In a storm-relative environment of a traditional right-moving supercell, as a Rear Flanking Downdraft (RFD) subsides into the environment below the supercell thunderstorm upstream (to the west) of the mesocyclone (a) it brings mid-level momentum to the surface (b) where, along the outflow boundary, the ambient vertical wind shear is focused as an arched vortex sheet with positive vertical vorticity along the gust front (c). The vertical orientation and arching of the sheet is a consequence of the density current leading head's circulation.

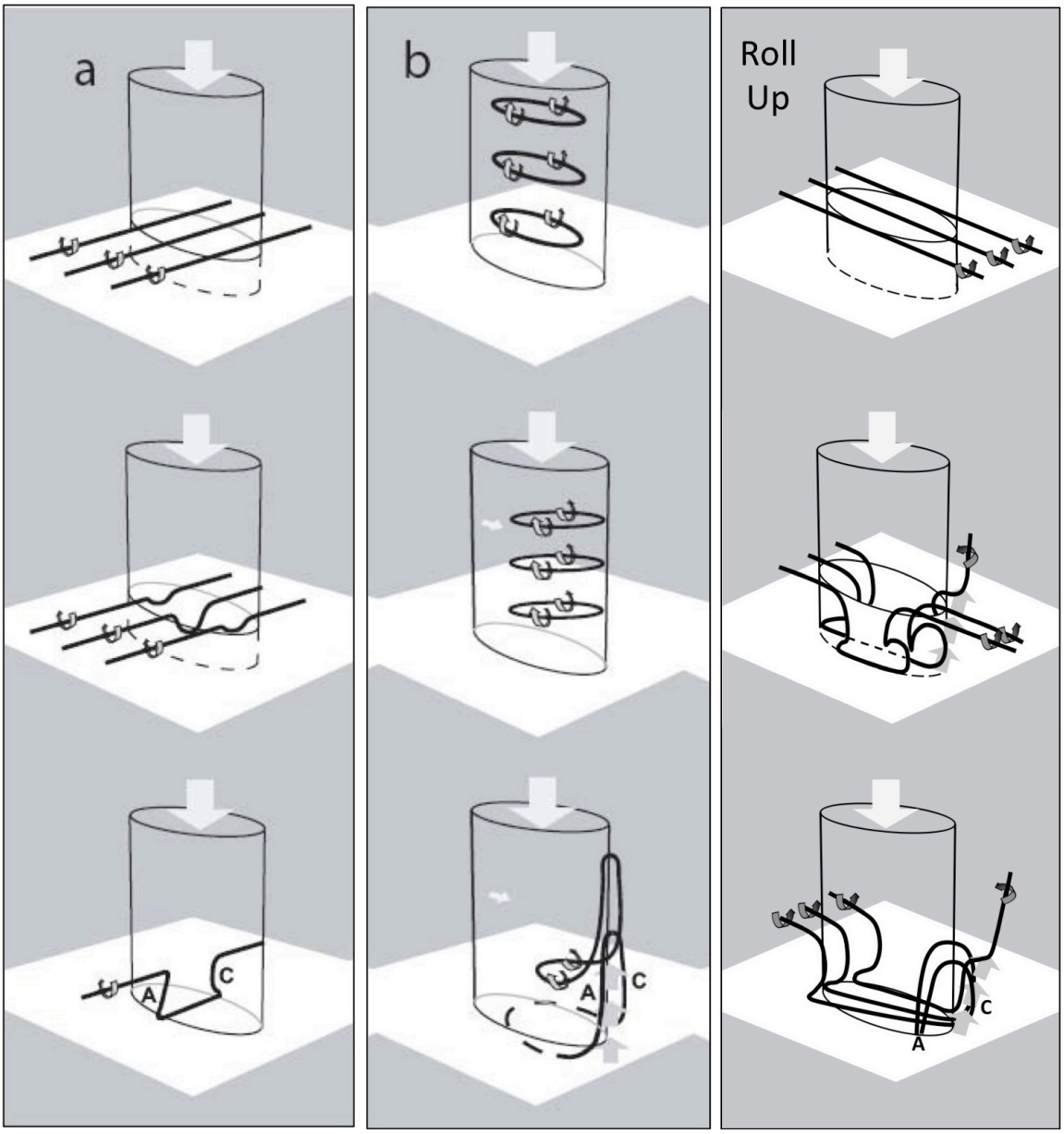

Figure 6.2: (a) see Figure 1.1a. (b) See Figure 1.1b. (Roll Up) A conceptual model built to represent the pre-tornadogenesis dynamics proposed in this text using vortex lines. As a downdraft subsides into a storm-relative environment characterized by positive low-level SRH, wind shear and helicity tilting by the downdraft yields a vertically erect vortex sheet along the outflow's gust front that arches back over the cold pool. As the vortex sheet rolls-up, support from the low-level SRH helps intensify resulting vortex tubes that are situated beneath the mesocyclone aloft. This acts to aggregate surrounding low-level vertical vorticity at the same time that the vortex arches become more vertically erect, due to updraft stretching. The consequent distribution of low-level vorticity is then a couplet of cyclonic and anticylonic vorticity that straddles the surface cold pool and is associated with vertically arching vortex lines.

REFERENCES

Arakawa, A., and V. Lamb, 1981: Potential enstrophy and energy conserving scheme for the shallow water equations. *Mon. Weather Rev.,* **109**, 18–36.

Barcilon, A., and P. G. Drazin, 1972: Dust devil formation. *Geophys. Fluid Dyn*., **4**, 147–158.

Barnes, S. L., 1970. Some aspects of a severe, right-moving thunderstorm deduced from mesonetwork rawinsonde observations. *J. Atmos. Sci*. **27**, 634–648.

Batchelor, G. K., 1967: *An Introduction to Fluid Dynamics*. Cambridge University Press, 516 pp.

Bluestein, H. B., 1980: The University of Oklahoma Severe Storms Intercept Project 1979. *Bull. Amer. Meteor. Soc*., **61**, 560–567.

——, 1985: The formation of a ‘‘landspout’’ in a ‘‘broken-line’’ squall line in Oklahoma. Preprints, *14th Conf. on Severe Local Storms, Indianapolis,* IN*,* Amer. Meteor. Soc., 267–270.

——, S. G. Gaddy, D. C. Dowell, A. L. Pazmany, J. C. Galloway, R. E. McIntosh, H. Stein, 1996: Doppler radar observations of substorm-scale vortices in a supercell. *Mon.. Wea. Rev.,* **125**, 1046-1059.

——, and ——, 2001: Airborne pseudo-dual-Doppler analysis of a rear-inflow jet and deep convergence zone within a supercell. *Mon. Wea. Rev*, **129** , 2270-2289.

——, C. C. Weiss, A. L. Pazmany, 2003: Mobile Doppler Radar Observations of a Tornado in a Supercell near Bassett, Nebraska, on 5 June 1999. Part I: Tornadogenesis. *Mon. Wea. Rev.*, **131**, 2954–2967.

——, 2010: History of tornado research. Preprints, *25th Conf. on Severe Local Storms*. Amer. Meteor. Soc., Denver, CO.

Bradford, M., 1999: Historical Roots of Modern Tornado Forecasts and Warnings. *Wea. Forecasting*, **14**, 484–491.

Brandes, E. A., 1984: Vertical vorticity generation and mesocyclone sustenance intornadic thunderstorms: The observational evidence. *Mon. Wea. Rev*, **112**, 2253-2269.

Browning, K. A., and R. J. Donaldson, 1963: Airflow and structure of a tornadic storm. *J. Atmos. Sci.,* **20**, 533–545

Byers, H. R. and R. R. Braham, Jr., *The Thunderstorm: Final Report of the Thunderstorm Project* (Washington, DC: U.S. Government Printing Office, 1949). This 282 page book is a comprehensive report of both the results of the project and the technology and observational techniques used.

Brooks, H. E., C. A. Doswell III, and R. P. Davies-Jones, 1993: Environmental helicity and the maintenance and evolution of low-level mesocyclones. *The Tornado: Its Structure, Dynamics, Prediction, and Hazards*, C. Church, D. Burgess, C. Doswell and R. Davies-Jones, Eds., Amer. Geophys. Union, 97–104.

Church, C. R., J. T. Snow, G. L. Baker, E. M. Agee, 1979: Characteristics of Tornado Like Vortices as a Function of Swirl Ratio: A Laboratory Investigation. *J. Atmos. Sci.*, **36**, 1755–1776

Craven, J. P., and H. E. Brooks, 2004: Baseline climatology of sounding derived parameters associated with deep, moist convection. *Natl. Wea. Dig.,* **28**, 13–24.

Corfidi, S. F., 1999: The Birth and Early Years of the Storm Prediction Center. *Wea. Forecasting*, **14**, 507–525.

Darkow, G. L., and D. W. McCann, 1977: Relative environmental winds for 121 tornado bearing storms. Preprints, *10th Conf. on Severe Local Storms*, Omaha, NE, Amer. Meteor. Soc., 413 – 417.

Davies-Jones, R. P., 1973: The Dependence of Core Radius on Swirl Ratio in a Tornado Simulator. *J. Atmos. Sci.*, **30**, 1427–1430.

——, 1982a: A new look at the vorticity equation with application to tornadogenesis. Preprints, *12th Conf. on Severe Local Storms, San Antonio*, TX, *Amer. Meteor. Soc*, 249–252.

——, 1982b: Observational and theoretical aspects of tornadogenesis. *Intense Atmospheric Vortices*, L. Bengtsson and J. Lighthill, Eds., Springer-Verlag, 175–189.

——, 1984: Streamwise Vorticity: The Origin of Updraft Rotation in Supercell Storms. *J. Atmos. Sci.*, **41**, 2991–3006.

——, and Brooks, H. E., 1993: Mesocyclogenesis from a theoretical perspective. Tornadoes and tornadic storms: a review of conceptual models. *The Tornado: Its Structure, Dynamics, Prediction, and Hazards*, C. Church, D. Burgess, C. Doswell and R. Davies-Jones, Eds., Amer. Geophys. Union, **79**, 105-114.

——, R. J. Trapp, and H. B. Bluestein, 2001: Tornadoes and tornadic storms. *Severe Convective Storms, Meteor. Monogr.,* Amer. Meteor. Soc., **50,** 167–222.

——, P. Markowski, 2013: Lifting of Ambient Air by Density Currents in Sheared Environments. *J. Atmos. Sci.*, **70**, 1204–1215.

Desai, B. N.. and S. Mal, 1938: Thundersqualls of Bengal, Getlairds Beit. z. Geophys., **53**, 285-304.

Doswell, C. A III; S. J. Weiss and R. H. Johns, 1993: Tornado Forecasting: A review. *The Tornado: Its Structure, Dynamics, Prediction, and Hazards*, C. Church et al., Eds., Geophys. Mon. **79**, Amer. Geophys. Union, 557-571.

——, 2007: Historical over view of severe convective storms research. *Electron. J. Severe Storms Meteor* **2**, 1–25.

Drazin, P. G., and L. N. Howard, 1966: Hydrodynamic stability of parallel flow of inviscid fluid. *Advances in Applied Mechanics*, G. G. Chernyi, Ed, Vol. 9, Academic Press, 1–89.

Ferreira, R. N., and W. H. Schubert, 1997: Barotropic Aspects of ITCZ Breakdown. *J. Atmos. Sci.*, **54**, 261–285.

Finley, J. P., 1884: Tornado predictions. *Amer. Meteor. J.,* **1**, 85-88.

——, 1888: Tornadoes. First prize essay, *Amer. Meteor. J.,* **5**, 165-179.

French, M. M., H. B. Bluestein, I. PopStefanija, C. A. Baldi, and R. T. Bluth, 2013: Reexamining the Vertical Development of Tornadic Vortex Signatures in Supercells. *Mon. Wea. Rev.*, **141**, 4576–4601.

Fujita, T. T., 1960: A Detailed Analysis of the Fargo tornadoes of June 20, 1957. USWB Research Paper No. 42, Washington, D.C., 67 pp. [out of print]

——, 1973: Tornadoes around the world. *Weatherwise*, **26**, 56-83

——, 1985: *The downburst. Satellite and Mesometeorology Research Project*, University of Chicago, 122 pp.

Gall, R. L., 1983: A linear analysis of the multiple vortex phenomenon in simulated tornadoes. *J. Atmos. Sci.,* **40,** 2010-2024.

Golden, J. H., 1971: Waterspouts and Tornadoes over south Florida1. *Mon. Wea. Rev.*, **99**, 146–154

——, 1974: The Life Cycle of Florida Keys' Waterspouts. I. *J. Appl. Meteor.*, **13**, 676–692.

Galway, J. G., and J. P. Finley, 1985: The First Severe Storms Forecaster. *Bull. Amer. Meteor. Soc.*, **66**, 1389–1395.

Grice, G. K., and Coauthors, 1999: The Golden Anniversary Celebration of the First Tornado Forecast. *Bull. Amer. Meteor. Soc.*, **80**, 1341–1348.

Grzych, M. L., B. D. Lee, and C. A. Finley, 2007: Thermodynamic analysis of supercell rear-flank downdrafts from Project ANSWERS. *Mon. Wea. Rev*., **135**, 240–246.

Guinn, T. A., and W. H. Schubert, 1993: Hurricane spiral bands. J. Atmos. Sci., **50**, 3380–3403.

Humphreys, W. J., 1940: Physics of the air, McGraw-Hill Book Co., Eds., pp. 353 and 359 .

Klemp, J. B., and R. Rotunno, 1983: A Study of the Tornadic Region within a Supercell Thunderstorm. *J. Atmos. Sci.*, **40**, 359–377.

Krasny, R., 1988: Computation of vortex sheet roll-up, Proceedings of the *UCLA Workshop on Vortex Methods*, C. R. Anderson, C. Greengard, Eds., *Lecture Notes in Mathematics,* Springer, **1360**, 9-22.

Lin, Y. J., and P. T. Chang, 1977: Some Effects of the Shearing and Veering EnvironmentalWind on the Internal Dynamics and Structure of a Rotating Supercell Thunderstorm. *Mon. Wea. Rev.*, **105**, 987–997.

Lee, B. D., and R. Wilhelmson 1997a: The numerical simulation of nonsupercell tornadogenesis. Part I: Initiation and evolution of pretornadic misocyclone circulations along a dry outflow boundary. *J. Atmos. Sci.,* **54**, 32–60.

——, and ——, 1997b: The Numerical Simulation of Nonsupercell Tornadogenesis. Part II: Evolution of a Family of Tornadoes along a Weak Outflow Boundary. *J. Atmos. Sci.*, **54**, 2387–2415.

——, C. A. Finley, and C. D. Karstens: 2012: The Bowdle, South Dakota, cyclic tornadic supercell of 22 May 2010: Surface analysis of rear-flank downdraft evolution and multiple internal surges. *Mon. Wea. Rev.,* **140**, 3419-3441.

Leslie, L. M., and R. K. Smith, 1978: The Effect of Vertical Stability on Tornadogenesis. *J. Atmos. Sci.*, **35**, 1281–1288.

Lewellen, D. C., and W. S. Lewellen, 2007: Near-Surface Intensification of Tornado Vortices. *J. Atmos. Sci.*, **64**, 2176–2194

Louis, J. F., 1979: A parametric model of vertical eddy fluxes in the atmosphere. *Bound. Layer Meteor*., **17**, 187–202.

Maddox, R. A., 1976: An Evaluation of Tornado Proximity Wind and Stability Data. *Mon. Wea. Rev.*, **104**, 133–142.

Marchand, M., 1993: Mankaya and the Kiowa Indians: Survival, Myth and the Tornado. *Heritage of the Great Plains,* Emporia State University, Eds., **26**, pp 19.

Markowski, P. M., J. M. Straka, and E. Rasmussen, 2002: Direct surface thermodynamic observations within the rear-flank downdrafts of nontornadic and tornadic supercells. *Mon. Wea.Rev.,* **130**, 1692–1721.

——, C. Hannon, J. Frame, E. Lancaster, A. Pietrycha, R. Edwards, and R. L. Thompson, 2003: Characteristics of Vertical Wind Profiles near Supercells Obtained from the Rapid Update Cycle. *Wea. Forecasting*, **18**, 1262–1272.

——, E. N. Rasmussen, J. M. Straka, R. P. Davies-Jones, Y. Richardson, and J. Trapp, 2008: Vortex lines within lowlevel mesocyclones obtained from pseudo-dual Doppler radar observations. *Mon. Wea. Rev*., **136**, 3513–3535.

——, and Y. P. Richardson, 2009: Tornadogenesis: Our current understanding, forecasting considerations, and questions to guide future research. *Atmos. Res.*, **93**, 3–10.

——, and Y. P. Richardson, 2010: Density current dynamics. *Mesoscale meteorology in midlatitudes*. J. Wiley & Sons, Ed., Wiley-Blackwell, 142-149.

——, Y. Richardson, J. Marquis, R. P. Davies-Jones, J. Wurman, K. Kosiba, P. Robinson, E. N. Rasmussen, and D. Dowell, 2012a: The pretornadic phase of the Goshen County, Wyoming, supercell of 5 June 2009 intercepted by VORTEX2. Part I: Evolution of kinematic and surface thermodynamic fields. *Mon. Wea. Rev.,* **140**, 2887–2915.

——, Y. Richardson, J. Marquis, R. P. Davies-Jones, J. Wurman, K. Kosiba, P. Robinson, E. N. Rasmussen, and D. Dowell, 2012b: The pretornadic phase of the Goshen County, Wyoming, supercell of 5 June 2009 intercepted by VORTEX2. Part II: Intensification of Low-level Rotation. *Mon. Wea. Rev.,* **140**, 2916-2938.

Marquis, J. N., Y. P. Richardson, J. M. Wurman, 2007: Kinematic Observations of Misocyclones along Boundaries during IHOP. *Mon. Wea. Rev.*, **135**, 1749–1768.

——, Y. Richardson, P. M. Markowski, D. Dowell, and J. Wurman, 2012: Tornado maintenance investigated with high-resolution dual-Doppler and EnKF analysis. *Mon. Wea. Rev*., **140**, 3–27.

Maxworthy, T., 1973: A Vorticity Source for Large-Scale Dust Devils and Other Comments on Naturally Occurring Columnar Vortices. *J. Atmos. Sci.*, **30**, 1717 1722.

Mitchell, K. E., and J. B. Hovermale, 1977: A Numerical Investigation of the Severe Thunderstorm Gust Front. *Mon. Wea. Rev.*, **105**, 657–675.

Newton, C. W., 1950: Structure and mechanism of the prefrontal squall line, *J. Met.,* **7**, 210—222.

——, and S. Katz, 1958: Movement of large convective rainstorms in relation to winds aloft, *Bul. Amer. Met. Sec*., **39**, 129-136.

——, and H. R. Newton, 1959: Dynamical interactions between large convective clouds and environment with vertical shear, *J. Met*., **16**, 483-496.

Noda, A. T., and H. Niino, 2005: Genesis and structure of a major tornado in a numerically-simulated supercell storm: Importance of vertical vorticity in a gust front. *Sci. Online Lett. Atmos.*, **1,** 5–8.

Noda, A. T., and H. Niino, 2010: A numerical investigation of a supercell tornado: Genesis and vorticity budget. *J. Meteor. Soc. Japan,* **88**, 135-159.

Nolan, S., 2006: Why the swirl ratio is a useless parameter. Poster, *86th AMS Annual Meeting, Atlanta,* GA, Amer. Met. Soc.

Odell, L. E., G. J. Tripoli, S. T. Trevorrow, and M. L. Büker, 2014: Vortex genesis and intensification processes associated with an idealized tornadic supercell. Poster, *94th AMS Annual Meeting, Atlanta,* GA, Amer. Met. Soc.

Orf, L. G., and J. R. Anderson, 1999: A numerical study of travelling microbursts. *J. Atmos. Sci.,* **127**, 1244–1258.

Proctor, F. H., 1988: Numerical Simulations of an Isolated Microburst. Part I: Dynamics and Structure. *J. Atmos. Sci.*, **45**, 3137–3160.

Ray, P. S., R. J. Doviak, G. B. Walker, D. Sirmans, J. Carter, B. Bumgarner, 1975: Dual Doppler Observation of a Tornadic Storm. *J. Appl. Meteor.*, **14**, 1521–1530.

——, 1976: Vorticity and Divergence Fields within Tornadic Storms from Dual-Doppler Observations. *J. Appl. Meteor.*, **15**, 879–890.

Rayleigh, Lord, 1880: On the stability, or instability, of certain fluid motions. *Proc. London Math. Soc*., **11**, 57–70.

Reynolds, O., 1883: An experimental investigation of the circumstances which determine whether the motion of water shall be direct or sinuous, and of the law of resistance in parallel channels. *Phil. Trans. of the Royal Soc.,* **174**, 935–982.

Rotunno, R., 1977: Numerical Simulation of a Laboratory Vortex. *J. Atmos. Sci.*, **34**, 1942–1956.

——, 1978: Note on the stability of a cylindrical vortex sheet. *J. Fluid Mech.*, **87,** 761 771.

——, 1982: Numerical simulation of multiple vortices. *Topics in Atmospheric and Oceanic Science: Intense Atmospheric Vortices*, L. Bengtsson and M. J. Lighthill, Eds., Springer-Verlag 117-215.

——, and J. Klemp, 1985: On the rotation and propagation of simulated supercell thunderstorms. *J. Atmos. Sci.,* **42**, 271-292.

Schaefer, J. T., 1986: Severe thunderstorm forecasting: A historical perspective. *Wea. Forecasting*, **1**, 164-189.

Shabbott, C. J., and P. M. Markowski, 2006: Surface in situ observations within the outflow of forward-flank down drafts of supercell thunderstorms. *Mon. Wea. Rev*., **134**, 1422–1441.

Stokes, G., 1851: On the Effect of the Internal Friction of Fluids on the Motion of Pendulums. *Phil. Trans. of the Royal Soc*., **9**, 8–106.

Straka, J. M., E. N. Rasmussen, R. P. Davies-Jones, and P. Markowski, 2007: An observational and idealized numerical examination of low-level counter-rotating vortices toward the rear flank of supercells. *Electron. J. Severe Storms Meteor.,* **2**, 1–22.

Thompson, R. L., R. Edwards, J. A. Hart, K. L. Elmore, and P. M. Markowski, 2003: Close proximity soundings within supercell environments obtained from the rapid update cycle. *Wea. Forecasting*, **18**, 1243–1261.

Trapp, J. R., Davies-Jones R., 1997: Tornadogenesis with and without a Dynamic Pipe Effect. *J. Atmos. Sci.*, **54**, 113–133.

Tripoli, G. J. and E. A. Smith, 2014a: Introducing Variable-Step Topography (VST) Coordinates within Dynamically Constrained Nonhydrostatic Modeling System (NMS). Part 1: VST Formulation within NMS Host Model Framework. *Dynamics of Atmospheres and Oceans*, Elsevier, In press.

Tripoli, G. J. and E. A. Smith, 2014b: Introducing Variable-Step Topography (VST) Coordinates within Dynamically Constrained Nonhydrostatic Modeling System (NMS). Part 2: VST Performance on Orthodox Obstacle Flows . *Dynamics of Atmospheres and Oceans,* Elsevier, In press.

Wakimoto, R. M., C. Liu, and H. Cai, 1998: The Garden City, Kansas, storm during VORTEX 95. Part I: Overview of the storm's life cycle and mesocyclogenesis. *Mon. Wea. Rev*., **126** , 372-392.

——, and J. W. Wilson, 1989: Non-supercell Tornadoes. *Mon. Wea. Rev.*, **117**, 1113 1140.

——, and H. Cai, 2000: Analysis of a nontornadic storm during VORTEX 95. *Mon. Wea. Rev*., **128**, 565-592.

Walko, R. L., 1993: Tornado spin-up beneath a convective cell: Required basic structure of the near-field boundary layer winds. *The Tornado: Its Structure, Dynamics, Prediction, and Hazards*, C. Church, D. Burgess, C. Doswell and R. Davies Jone*s,* Eds., Amer. Geophys. Union, 89–95.

Ward, N. B., 1961: Radar and surface observations of tornadoes of May 4, 1961. Proc. Ninth Weather Radar Conf., Kansas City, MO, Amer. Meteor. Soc., 175–180.

——, 1972: The explanation of certain tornado dynamics using a laboratory model. *J. Atmos. Sci.,* **49**, 1194-1204.

Weisman, M. L., and J. B. Klemp, 1981: The effects of directional turning of the low level wind shear vector on modeled multicell and supercell storms. *Bull. Amer. Meteor. Soc.,* **62**, 1425-1425.

Wu, J. Z., H. Y. Ma and M. D. Zhou, 2006: *Vorticity and Vortex Dynamics.* Springer, 473 pp.